Pontificia Universidad Católica de Chile
Faculty of Physics
Institute of Astrophysics

New Constraints For The Initial-to-Final Mass Relation Of White Dwarfs

by

Manuel Hernán Barrientos Laurence

Thesis submitted to the Faculty of Physics
of Pontificia Universidad Católica de Chile,
one of the requirements to qualify for the
academic Master's degree in Astrophysics

Supervisor	:	Dr. Julio Chanamé (PUC, Chile)
Committee	:	Dr. Márcio Catelan (PUC, Chile)
		Dr. Claudia Aguilera (Univ. Andres Bello, Chile)

April, 2020

Santiago, Chile

Acknowledgements

I wish to express my deepest gratitude to my supervisor, Dr. Julio Chanamé, who has been an excellent ”coach” during these years. He guided me, encouraged me, and most importantly he believed in me and my work.

I wish to acknowledge the support and great love of my family, friends, and basketball. They kept me going on through tough times and this work would not have been possible without them.

I would like to pay my special regards to my working group at PUC led by Dr. Julio Chanamé, every Tuesday morning meeting was helpful and fun. Also, I want to thank Jeff Andrews and Claudia Aguilera for helping me in moments of despair.

Contents

Abstract

We present observational constraints for the initial-to-final mass relation (IFMR) derived from 11 white dwarfs (WDs) in wide binaries (WBs) that contain a turnoff/subgiant primary. Because the components of WBs are coeval to a good approximation, the age of the WD progenitor (and hence its mass) can be determined from the study of its wide companion. However, previous works that used wide binaries to constrain the IFMR suffered from large uncertainties in the initial masses because their MS primaries are difficult to age-date with good precision. Our more careful selection of wide binaries with evolved primaries avoids this problem by restricting to a region of parameter space where isochrone ages are significantly easier to determine with precision. We selected a sample of wide binary systems with adequate characteristics for our program by matching existing catalogs of WDs with the Gaia astrometric surveys. Atmospheric parameters, masses and cooling times for the WDs were taken from the literature, while we obtained high-resolution spectra of the primaries in order to determine their stellar parameters and total ages. We obtained more precise constraints than existing ones in the mass range 1-2.5 $M_{\odot}$, corresponding to a previously poorly/sparsely constrained region of the IFMR. Having introduced the use of wide subgiant-WD binaries, the study of the IFMR of WDs is not limited anymore by the precision in initial mass, but now the pressure is on final mass, i.e., the mass of the WD today. Our results indicate a non-negligible spread in WD final masses within this initial-mass range. As already noted, improved determinations of the masses of the WDs in this regime would be important for settling this question.

Chapter 1

Introduction

1.1 Initial-to-Final Mass Relation of White Dwarfs

Stars with initial masses below 8-10 $M_\odot$ will one day evolve into white dwarfs (WDs), the evolutionary endpoint of over 97 % of the stars in our galaxy. The properties of WD progenitors during their main-sequence (MS) lifetimes are theoretically very well understood and observationally very well constrained. Similarly, once the WD is born, its subsequent evolution is straightforward and governed by simple cooling by radiation from its surface. However, many aspects of the star's evolution from the tip of the red giant branch (RGB) to its landing on the WD cooling sequence remain elusive. In particular, during the thermally pulsing asymptotic giant phase (TP-AGB), these stars will go through multiple pulses that expel their outer shells, shedding an important percentage of their mass (Weidemann, 1993, 2000). Taking this into account, we do not know how much mass is lost between those evolutionary points for a given progenitor mass (not to speak about metallicity effects). Such mapping determines what is known as the initial-to-final mass relation (hereafter IFMR) of WDs. The IFMR seeks to answer a simple question: what is the mass of the WD a given progenitor star will produce? This relationship quantifies the mass lost by a star over its lifetime and therefore has implications on wide-ranging astronomical phenomena from the pathways that produce Type Ia supernovae to the future evolution of our Solar System (Williams et al., 2009).

Previous studies starting with the empirical approach by Weidemann (1977) to the latest researches have helped us understand the IFMR, but there are still some pieces missing in the puzzle. For example, the dependence of this function on different parameters as the metallicity, magnetic field, and rotation is not clear. Numerous works have dealt with the calculation of a theoretical IFMR (e.g. Dominguez et al., 1999; Weiss and Ferguson, 2009; Choi et al., 2016), but the differences in their evolutionary codes such as the treatment of convection, the value of the assumed critical mass; which is the maximum mass of a white dwarf progenitor, or the mass-loss prescriptions used lead to very different results; especially after the first thermal pulse in the AGB. From an observational perspective, most efforts up to now have focused on the observation of WDs in open clusters (OCs), since this allows to infer the total age and the original metallicity of WDs belonging to the cluster (Kalirai et al., 2005). OCs have made possible the derivation of a semi-empirical IFMR, although only covering the initial mass range between 2.5 and 7.0 $M_{\odot}$ because these stellar clusters are relatively young, hence the WD progenitors in these clusters are generally massive. A parallel attempt to cover the low-mass range of the IFMR was carried out by Catalán et al. (2008b). This was the first study of this relationship based on common proper motion pairs. This method allows a better spectroscopic study of the pair given its distance in comparison with star clusters. At the same time, the study of these pairs enables a wide age and metallicity coverage of the IFMR. Lately, new approaches to constraint the IFMR have been developed by Andrews et al. (2015) and El-Badry et al. (2018), using wide WD-WD binaries and field WDs in *Gaia* respectively; both works found interesting results for solar metallicity.

1.2 Semi-Empirical Determination of the Initial-to-Final Mass Relation

Semi-empirically constraining the IFMR requires the determination of the present masses of WDs and the initial masses of their progenitors. The former can be measured today via several observational techniques, but the latter is not directly measurable as the original star does not exist anymore. Therefore, the typical methodology is to obtain the total age of the WD and use stellar evolution models to trace back the mass of the WD progenitor. WD's masses and cooling times are typically determined by mapping effective temperatures and surface gravities into appropriate WD's cooling sequences; while the WD's total age is the sum of two lifetimes: that of its progenitor ($\tau_{\rm prog}$) and its cooling time ($\tau_{\rm cool}$) as we can see in Eq. 1.1. The progenitor lifetimes can be mapped easily to stellar masses with the aid of evolutionary models and knowledge of the metallicities.

$$\begin{aligned} \text{Total Age}_{\rm WD} &= \tau_{\rm prog} + \tau_{\rm cool} \ , \\ \tau_{\rm prog} &= \text{Total Age}_{\rm WD} - \tau_{\rm cool} \ . \end{aligned} \tag{1.1}$$

1.2.1 Using Open Clusters

Since stellar ages are most readily obtained for coeval groups of stars, WDs in stellar clusters have often been used to constrain the IFMR (Kalirai et al., 2005; Dobbie et al., 2006; Cummings et al., 2018). The comparison of a WD's cooling time to its cluster's age provides the necessary information to infer the initial mass of the WD's progenitor. In this case, we can adapt Eq. 1.1 as follows

$$\begin{aligned} \text{Total Age}_{\rm WD} = \tau_{\rm prog} + \tau_{\rm cool} &= \text{Age}_{\rm OC} \ , \\ \tau_{\rm prog} &= \text{Age}_{\rm OC} - \tau_{\rm cool} \ . \end{aligned} \tag{1.2}$$

However, constraining the IFMR using OC's WDs is difficult. For accurate spectral determinations, only WDs in nearby OCs can place strong constraints. Moreover, these stellar groups tend to be young enough that lower mass stars have not evolved off the MS, making this method most sensitive to the high-mass end of the IFMR as can be seen in Fig. 1.1. Here, the grey dots show the constraints by Cummings et al. (2018) using OC's WDs, these points cover the initial mass space over 2.5 $M_\odot$ with metallicity values between -0.14 < [Fe/H] < +0.15.

In particular, stars in OCs tend to be metal rich, thus the constraints found using this method are limited because of the small metallicity coverage. It is known that this parameter is capable of affecting the evolution of a star, hence the resulting IFMR. For example, a theoretical study by Renedo et al. (2010) found that metal-poor stars yielded more massive WDs for a given progenitor mass. On the other hand, an observational study by Kalirai et al. (2007) found evidence for enhanced mass loss at extremely high metallicity stars. We will discuss more about the OCs constraints and metallicity effects in Section 4.2 and 4.3.

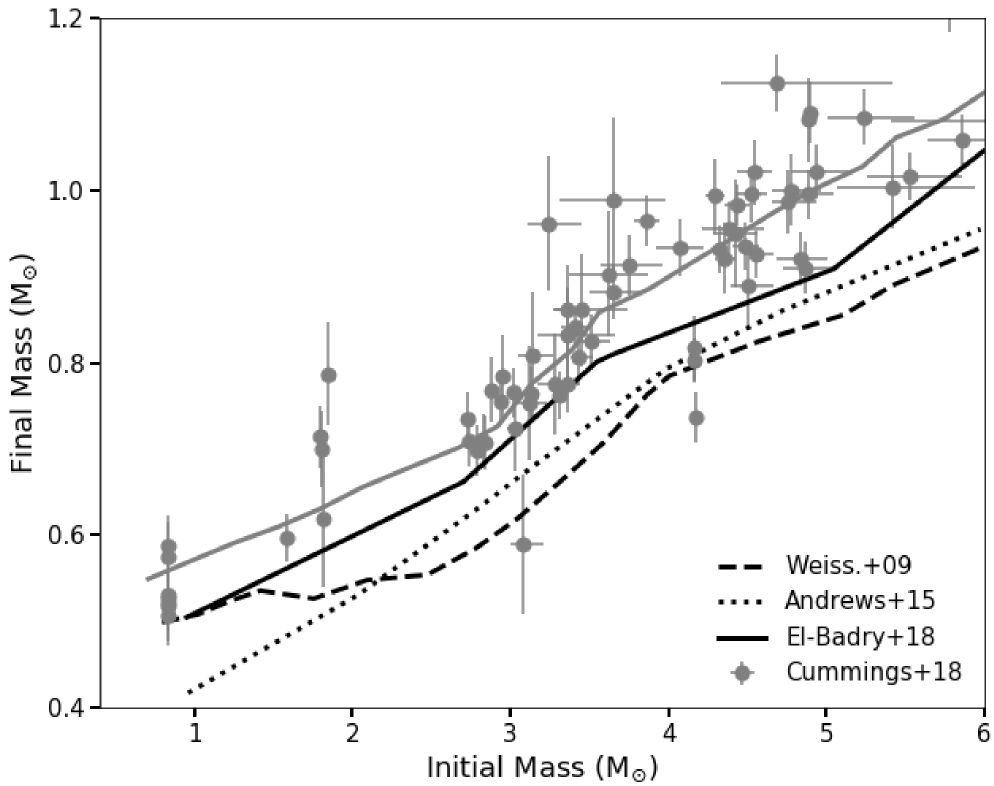

Figure 1.1: Empirical constraints on the initial-to-final mass relation of WDs presented in Cummings et al. (2018) using OCs. Grey dots are OCs constraints with their error bars, and the grey solid line is the fit to these data. Black solid line is the IFMR by El-Badry et al. (2018) using field WDs, black dotted line is the IFMR by Andrews et al. (2015) using wide WD-WD binaries and the black dashed line is a theoretical IFMR from Weiss and Ferguson (2009).

1.2.2 Using Wide Binaries

Wide binaries (WBs) containing at least one WD provide an alternative method for calibrating the IFMR. We can define a WB as a system of two stars whose properties are consistent with being gravitationally bound to each other, usually with orbital separations a $\gtrsim$ 100 AU (Andrews et al., 2017). The two components of a binary are expected to be coeval (Greenstein, 1986), and therefore these systems can be considered as the smallest possible examples of a star cluster; any property easily determined for one of the components (say, its age, metallicity) can be safely assigned to the other (Andrews et al., 2018, 2019). Using Eq. 1.1, the age relation between the primary and the secondary (always a WD) component of a WB can be represented as follows

$$\begin{aligned} \mathrm{Age}_{\mathrm{primary}} &= \mathrm{Age}_{\mathrm{secondary}} \ , \\ \mathrm{Age}_{\mathrm{primary}} &= \mathrm{Total\ Age}_{\mathrm{WD}} = \tau_{\mathrm{prog}} + \tau_{\mathrm{cool}} \ . \end{aligned} \tag{1.3}$$

For these systems, the coeval components are far enough apart that they can be assumed to have evolved in isolation (Silvestri et al., 2001). Thus, the components of WBs have not been subjected to mass transfer during their lifetimes. We know that binary systems with small separation (e.g, contact binaries) can interact and have mass transfer from one star to the other, changing their evolutionary process and composition. But for wide enough binaries we can consider that mass transfer is negligible (Andrews et al., 2015).

WBs that include a MS star and a WD have been used to constrain the IFMR (e.g. Catalán et al., 2008b; Zhao et al., 2012) as can be seen in Fig. 1.2. In this case, the constraints cover the initial mass space under 2.5 $M_\odot$ with metallicity values between -0.44 < [Fe/H] < +0.15. We notice that these constraints (grey squares) have big uncertainties in the initial mass determination, this is because of the low precision obtaining ages for MS stars via theoretical isochrones. Also, WBs containing two WDs have been used to study this relation as can be seen in Andrews et al. (2015), this work developed a statistical model that allows any well-characterized wide WD-WD binary to constrain the IFMR (dotted line in Fig. 1.2).

1.2.3 Using Turnoff/Subgiant-White Dwarf Binaries

In this thesis, we aim to provide new high-precision constraints on the IFMR of WDs by taking advantage of WBs selected such that stellar age determinations for these systems are very precise. For this, we selected pairs where the primary is an evolved turnoff (TO) or subgiant (SG) star and the secondary a WD. Therefore, using Eq. 1.3 we can write

$$\mathrm{Age}_{\mathrm{TO/SG}} = \mathrm{Total\ Age}_{\mathrm{WD}} = \tau_{\mathrm{cool}} + \tau_{\mathrm{prog}}. \tag{1.4}$$

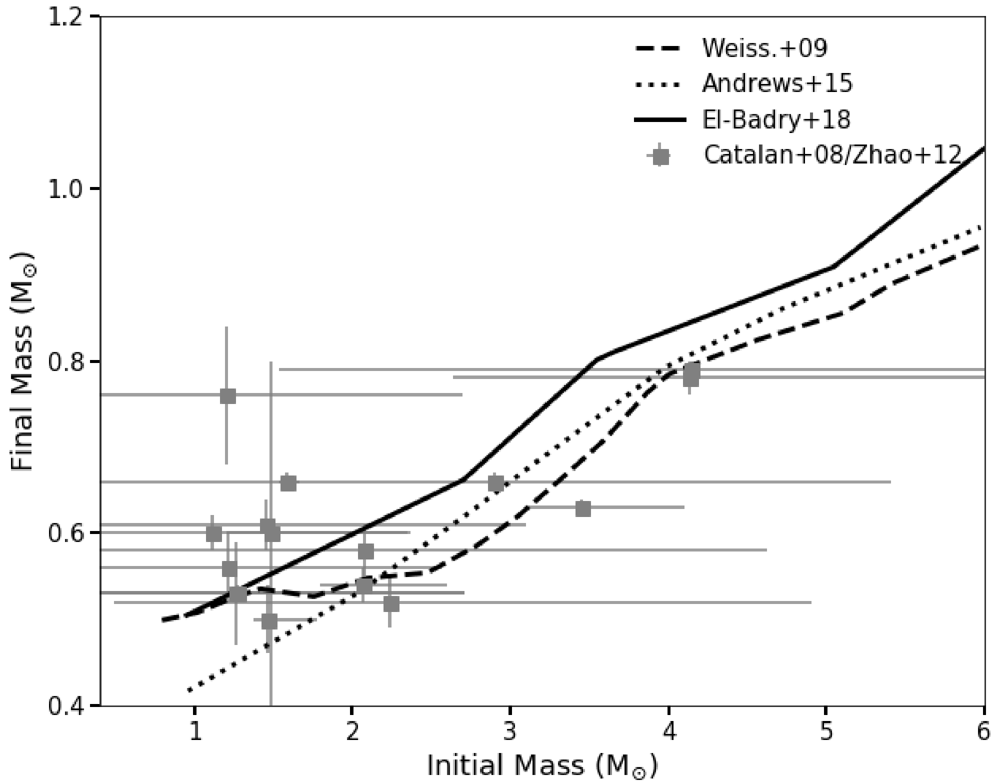

Figure 1.2: Semi-empirical constraints on the initial-to-final mass relation of WDs using WBs. Grey squares are constraints found by Catalán et al. (2008b) and Zhao et al. (2012). Black solid line is the IFMR by El-Badry et al. (2018) using field WDs, black dotted line is the IFMR by Andrews et al. (2015) using wide WD-WD binaries and the black dashed line is a theoretical IFMR from Weiss and Ferguson (2009).

In these WBs, the total age of the system, and thus of the WD, is obtained from the fitting of theoretical isochrones to the position of the TO/SG primary in a Hertzsprung-Russell (HR) diagram. It was demonstrated in Chanamé and Ramírez (2012) that the isochrone ages for TO/SG primaries have typical precision of better than about 15-20% with Hipparcos-class parallaxes. The expectation is that these new calibrators will help us to finally populate the low-mass end of IFMR ($M_i < 2.5$ $M_\odot$), with precise determinations of the initial masses in particular.

1.3 Structure

We begin by describing in Chapter 2 the results of a search for WBs with TO/SG primaries and WD secondaries, we also describe our observations and the data reduction. In Chapter 3 we present the determination of stellar atmospheric parameters for both WB components, ages of the primaries using theoretical isochrones and initial mass determination for WDs progenitors. In Chapter 4 we show and discuss the resulting constraints for the IFMR, concluding this thesis in Chapter 5.

Chapter 2

Target Selection and Observations

2.1 Searching for Wide Binaries: Turnoff/Subgiant-White Dwarfs

For true, gravitationally bound WBs, the component stars are expected to have the same 3D-positions and 3D-velocities, down to the level of their orbital sizes and velocities. In terms of typical observables, this translates into pairs of stars with matching positions, proper motions, parallaxes, radial velocities, and even metallicities depending on the data available and the precision of it (Godoy-Rivera and Chanamé, 2018).

In this work, we searched for WBs by matching positions, proper motions and parallaxes from the Tycho-Gaia Astrometric Solution (TGAS; Michalik et al., 2015) catalog, which contains the primaries of our binaries and the WD catalog from the Sloan Digital Sky Survey Data Release 12 (SDSS DR12; Kepler et al., 2016) containing the secondary stars. TGAS is a subset of *Gaia* Data Release 1 comprising those stars in the Hipparcos and Tycho-2 catalogs for which a full 5-parameter astrometric solution has been possible, this catalog has around 2 million stars. The WD catalog from SDSS DR12 is one of the largest available, we took advantage of Anguiano et al. (2017) work with a subsample of 20247 hydrogen rich (DA) WDs. This catalog has positions, proper motions, photometric distances, effective temperatures, surface gravities, masses, and cooling times. We do not have radial velocities for the WDs because it is not possible to measure it directly given the gravitational redshift effect. Not to speak of how hard (or impossible) it is to have WDs metallicities, hence we cannot cross-match these parameters. Given these data, we performed a search for WBs.

2.1.1 Astrometric Parameters and Criteria

For our search, we will only use those stars with proper motions (μ_α, μ_δ) and parallaxes (ϖ) well measured in our sample. For a given star, in order to quantify the quality of its proper motion and parallax, we have defined the (dimensionless) parameters:

$$\frac{\mu}{\sigma_\mu} = \frac{|\vec{\mu}|}{|\vec{\sigma_\mu}|} = \frac{\sqrt{\mu_\alpha^2 + \mu_\delta^2}}{\sqrt{\sigma_{\mu_\alpha}^2 + \sigma_{\mu_\delta}^2}} \qquad \text{and} \qquad \frac{\varpi}{\sigma_\varpi} \ , \tag{2.1}$$

where μ_α and μ_δ are the proper motions in right ascension (α) and declination (δ) respectively; μ_α already accounts for the multiplicative $\cos(\delta)$ factor. μ is the total proper motion, and σ_μ is the total proper motion error. On the other hand, ϖ is the parallax and σ_ϖ the error. Considering these new parameters, our first selection criterion applied to expedite the calculations and avoid unnecessary pair matching is:

$$\frac{\mu}{\sigma_\mu} \geq 3 \qquad \text{and} \qquad \frac{\varpi}{\sigma_\varpi} \geq 3 \ .$$

Our second selection parameter is related to the projected separation of our WBs:

$$s = \Delta\theta \times \ \mathrm{d} \ ,$$

where the distance d comes from the relation with the parallax ($\mathrm{d} \approx 1/\varpi$) and $\Delta\theta$ is the angular separation between stars. Given two stars A and B located nearby in the sky, we calculated the angular separation between them as follows:

$$\Delta\theta(A, B) \simeq \sqrt{(\alpha_A - \alpha_B)^2 \cos\delta_A \cos\delta_B + (\delta_A - \delta_B)^2} \ ; \tag{2.2}$$

for each possible pair, we used this value to calculate the projected separation. Pairs with projected separations smaller than 1 pc are likely gravitationally bound (Yoo et al., 2004; Jiang and Tremaine, 2010), over this limit it is less probable and may be associated with dissolving clusters (Kouwenhoven et al., 2010). Andrews et al. (2017) argue that pairs beyond the Galactic tidal limit (or Jacobi radius, which is around 2 pc for ≈ 1 $\mathrm{M}_\odot$ stars within the solar neighborhood) should not be confused with genuine WBs. Moreover, Andrews et al. (2017) proposes that randomly aligned pairs selected from TGAS typically have s $> 4 \times 10^4$ AU, while pairs under this threshold are mostly genuine. However, the transition between genuine pairs and random alignments is not sharp. Under this mark, the contamination level is around 5%. Taking this into account, we limited our search to projected separations s $\lesssim 10^5$ AU. Pairs between this limit and s $> 4 \times 10^4$ AU will be carefully treated. Then, our second selection criterion is:

$$s \lesssim 10^5 \text{ AU} .$$

To be sure that these systems are WBs, we need both stars to move in the same direction at a similar speed. For this, we compare each of their proper motion coordinates as follows:

$$\Delta\mu(A,B) = |\vec{\mu_A} - \vec{\mu_B}| = \sqrt{(\mu_{\alpha,A} - \mu_{\alpha,B})^2 + (\mu_{\delta,A} - \mu_{\delta,B})^2} \; ; \tag{2.3}$$

to pass this cut, our pairs must have a difference in μ under 10 mas yr^{-1}. Therefore, our third criterion is:

$$\Delta\mu(A,B) \leq 10 \text{ mas yr}^{-1} .$$

Another important parameter that helps us to know if a pair is a true WB is the parallax. We need both stars to be at a similar distance from us. Hence, the difference between ϖ_A and ϖ_B has to be less than $3\sigma_{\varpi_{\rm AB}}$, where the $\sigma_{\varpi_{\rm AB}}$ considered here is a combinations in quadrature of both errors $\sigma_{\varpi_{\rm A}}$ and $\sigma_{\varpi_{\rm B}}$. Thus, our fourth criterion is:

$$\Delta\varpi(A,B) = |\varpi_A - \varpi_B| \leq 3\sigma_{\varpi_{\rm AB}} .$$

Using these set of criteria, we found ≈200 WB candidates. It is important to mention that this search did not make any distinction in the evolutionary state of the primary. Consequently, we found pairs whose primaries are MS, TO, SG and giant stars.

For our purpose, we only need those pairs where the primary star is a TO or SG star, this will be our fifth selection criterion. To select this type of primaries, we used a CMD, where we included stars from the LSPM North Proper Motion Catalog (Lépine, 2005) to use as a background for identifying the MS, SG and giant branch. By doing this, we can have a priori knowledge of the evolutionary state of the stars.

We put our primaries in the diagram and select those that fall between the grey lines, as is shown in Figure 2.1 (observed sample). The solid line shows the limit with the MS stars, and the dashed line shows the limit with the red giant branch (RGB) stars. The size of our region is considering stars over the grey solid line and under the grey dashed line between $0 < \text{V-J} < 1.8$ in color and $0 < M_v < 6$ in absolute magnitude in the V-band. It is important to notice that these boundaries were chosen arbitrarily by eye, and it does not guarantee the complete exclusion of MS stars or giant stars. For our sample, we do not have stellar parameters measured as the effective temperature or metallicity, therefore it is difficult to fit an isochrone to these stars to be sure about their evolutionary stage; especially considering the age-metallicity degeneracy and the short period of time that stars expend in the TO and SG phase. Using this last criterion, our sample was reduced from ≈200 pairs to ≈60 pairs.

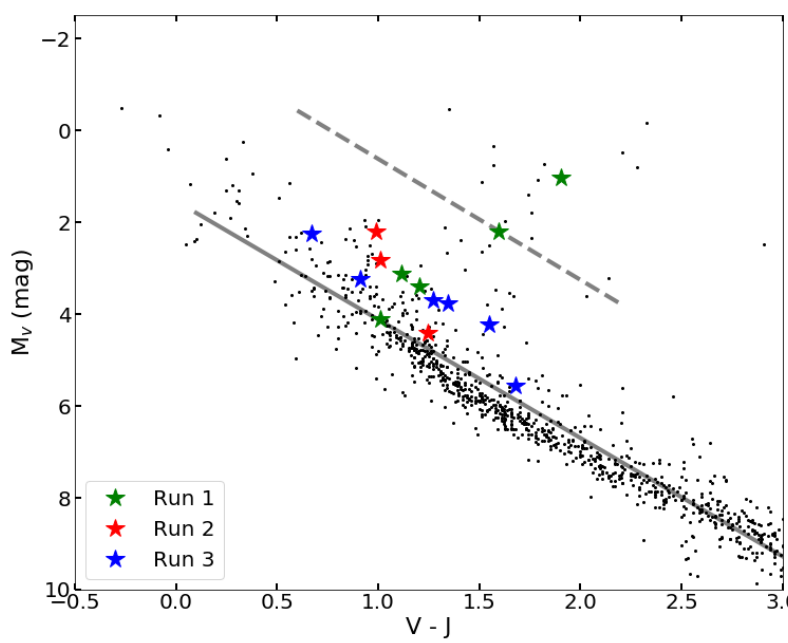

Figure 2.1: CMD showing the TO/SG selection. The background black dots are stars from Lépine (2005) Catalog. Green, red and blue stars show the position of our observed primaries. The grey lines show our limited space for TO and SG stars.

2.2 Observations and Data Reduction

For this thesis, our primary stars selected were observed with the high-resolution spectrograph MIKE (Bernstein et al., 2003) on the 6.5 m Clay Telescope at Las Campanas Observatory on July 25, 2017; October 01, 2018, and January 03, 2019. We used a narrow slit ($0.35''$), which delivers data with spectral resolution R = $\lambda/\Delta\lambda \simeq 65000$ (at $\lambda \simeq 6000$ Å) and the standard setup that allows complete wavelength coverage in the 3400-9100 Å spectral window.

2.2.1 First Observing Run

In this run, we observed 16 primaries of our WB candidates. We need to notice that at this time *Gaia* DR1 (Gaia Collaboration et al., 2016) was the latest data release, and our WDs had proper motions from USNO-B1 and photometric distances. For both components, the astrometric parameters were not as accurate as now with *Gaia* DR2, hence cross-matching slow proper motions, especially under 30 mas yr^{-1} could lead us to chance alignments, increasing the contamination in our sample. Consequently, for this run we used an extra criterion:

$$\mu_A, \mu_B \geq 30 \text{ mas yr}^{-1} \ .$$

Later, for this sample, we had to update the astrometric parameters for the primaries and secondaries because of *Gaia* DR2 (Gaia Collaboration et al., 2018), which has better and more accurate measurements. From the 16 WBs observed, just 5 of them passed all the cuts with the new astrometric data (green stars in Fig. 2.1). It is important to notice that for this run the grey dashed line in Fig. 2.1 was not considered in the target selection. Table 2.1 shows a comparison between older and new astrometric parameters for these 5 pairs. The WD SDSS J012824.93-082254.1 in Table 2.1 shows a big difference in parallax comparing USNO-B1 and *Gaia* DR2 values, about 2.5 mas. Despite this difference, this pair is still consistent with our criteria. It would be interesting to see if this value changes in future data releases.

Table 2.1: Wide Binaries Observed July 25, 2017: Proper Motion and Parallax Comparison

	Gaia DR1/USNO-B1			Gaia DR2		
Object ID	μ_α	μ_β	ϖ	μ_α	μ_β	ϖ
(TYC/SDSS)	(mas yr^{-1})	(mas yr^{-1})	(mas)	(mas yr^{-1})	(mas yr^{-1})	(mas)
5274-489-1	-61.33 ± 0.89	-170.26 ± 0.42	9.53 ± 0.34	-61.18 ± 0.09	-170.37 ± 0.06	9.46 ± 0.05
J012824.93-082254.1	-58.73 ± 2.36	-172.10 ± 2.36	10.04 ± 0.85	-61.87 ± 1.17	-172.43 ± 0.65	12.56 ± 0.59
1446-1524-1	-79.93 ± 0.79	-26.01 ± 0.51	3.97 ± 0.27	-76.02 ± 0.09	-22.55 ± 0.09	5.48 ± 0.08
J123604.65+170819.2	-74.54 ± 3.44	-22.61 ± 3.44	6.08 ± 0.80	-73.59 ± 0.60	-22.41 ± 0.41	4.91 ± 0.31
2033-5-1	4.38 ± 1.01	-46.64 ± 1.04	3.36 ± 0.28	3.19 ± 0.06	-47.41 ± 0.06	3.44 ± 0.04
J154634.50+233438.0	2.87 ± 2.82	-42.30 ± 2.82	6.10 ± 0.18	2.39 ± 0.24	-42.08 ± 0.23	4.44 ± 0.15
2229-1088-1	-25.54 ± 0.65	-36.16 ± 0.46	3.72 ± 0.43	-25.20 ± 0.06	-36.23 ± 0.05	3.42 ± 0.04
J225247.41+270433.7	-30.16 ± 2.58	-30.74 ± 2.58	2.86 ± 0.08	-23.71 ± 0.46	-27.86 ± 0.32	3.46 ± 0.24
558-2215-1	-17.57 ± 1.43	-25.48 ± 0.78	2.36 ± 0.41	-17.05 ± 0.07	-24.41 ± 0.07	1.93 ± 0.05
J220850.53+001349.0	-24.03 ± 5.15	-24.26 ± 5.15	0.90 ± 0.24	-24.03 ± 5.15	-24.26 ± 5.15	0.90 ± 0.57

2.2.2 Second and Third Observing Run

Before these two runs, we made a new search for WBs updating both catalogs used with the newest data release from *Gaia* DR2. In this new search, we used the same criteria shown in Section 2.1.1. This time, no extra criterion related to proper motion magnitude was used given the high quality of these astrometric parameters. We observed 9 new pairs, 3 in the second run and 6 in the third (red and blue stars in Fig.2.1, respectively).

The complete sample of WBs is in Table 2.2 with proper motions, parallaxes, magnitudes, angular separations, proper motions differences, and projected separations. The comparison of proper motions and parallaxes in terms of the projected separation in Fig. 2.2 for the whole sample. We used the catalog of WBs from Andrews et al. (2017) as a background in the latest figure.

Table 2.2: Wide Binaries in Our Sample: Turnoff/Subgiant Primary and White Dwarf Secondary

Pair N°	Object ID (TYC/SDSS)	μ_α (mas yr^{-1})	μ_β (mas yr^{-1})	ϖ (mas)	G (mag)	$\Delta\theta$ (arcsec)	$\Delta\mu$ (mas yr^{-1})	s (AU)
1	5274-489-1	-61.18 ± 0.09	-170.37 ± 0.06	9.46 ± 0.05	9.14	32.95	2.17	3483.15
	J012824.93-082254.1	-61.87 ± 1.17	-172.43 ± 0.65	12.56 ± 0.59	18.62			
2	1446-1524-1	-76.02 ± 0.09	-22.55 ± 0.09	5.48 ± 0.08	9.31	155.31	2.43	28325.65
	J123604.65+170819.2	-73.59 ± 0.60	-22.41 ± 0.41	4.91 ± 0.31	18.89			
3	2033-5-1	3.19 ± 0.06	-47.41 ± 0.06	3.44 ± 0.04	11.02	79.20	5.39	23030.50
	J154634.50+233438.0	2.39 ± 0.24	-42.08 ± 0.23	4.44 ± 0.15	17.96			
4	2229-1088-1	-25.20 ± 0.06	-36.23 ± 0.05	3.42 ± 0.04	9.35	311.69	8.49	91136.42
	J225247.41+270433.7	-23.71 ± 0.46	-27.86 ± 0.32	3.46 ± 0.24	18.30			
5	558-2215-1	-17.05 ± 0.07	-24.41 ± 0.07	1.93 ± 0.05	9.24	109.87	6.98	56957.23
	J220850.53+001349.0	-24.03 ± 5.15	-24.26 ± 5.15	0.90 ± 0.57	20.33			
6	595-764-1	-2.51 ± 0.12	-8.81 ± 0.07	3.52 ± 0.06	9.35	38.52	0.29	10948.15
	J001624.09+082157.0	-2.72 ± 0.60	-8.59 ± 0.36	3.76 ± 0.31	18.47			
7	38-358-1	39.02 ± 0.07	-4.34 ± 0.07	3.93 ± 0.04	11.28	216.22	3.43	55072.97
	J021134.67-000025.9	35.88 ± 0.66	-2.99 ± 0.54	3.70 ± 0.43	19.03			
8	5194-1015-1	39.18 ± 0.08	15.06 ± 0.07	2.31 ± 0.05	10.89	167.48	1.93	72441.59
	J211928.44-002632.9	39.21 ± 0.97	16.99 ± 0.91	2.02 ± 0.54	19.46			
9	823-447-1	-7.77 ± 0.09	3.85 ± 0.08	2.80 ± 0.05	11.23	52.15	1.28	18625.24
	J092228.57+121125.8	-8.54 ± 0.61	4.87 ± 0.51	2.81 ± 0.34	19.00			
10	1366-1363-1	-35.94 ± 0.08	-32.18 ± 0.04	6.91 ± 0.04	8.93	127.63	2.13	18478.24
	J075019.11+181356.9	-34.66 ± 0.29	-30.48 ± 0.18	6.96 ± 0.16	17.83			
11	4723-595-1	35.78 ± 0.06	15.05 ± 0.06	4.69 ± 0.04	11.55	18.35	0.46	3916.49
	J034315.83-060006.2	35.74 ± 0.32	14.59 ± 0.29	4.69 ± 0.18	17.89			
12	4969-457-1	-30.20 ± 0.09	0.64 ± 0.06	5.33 ± 0.05	8.57	95.91	0.59	18008.71
	J133619.70-025445.2	-30.69 ± 0.41	0.32 ± 0.23	5.47 ± 0.18	18.22			
13	4913-1024-1	-17.42 ± 0.07	-11.16 ± 0.07	5.17 ± 0.05	9.97	14.41	0.94	2786.59
	J104959.79-004719.1	-18.31 ± 0.28	-10.88 ± 0.24	5.18 ± 0.17	17.87			
14	1443-1882-1	10.03 ± 0.08	-38.19 ± 0.07	3.96 ± 0.06	10.68	14.72	0.55	3715.10
	J115357.30+190606.9	9.57 ± 0.52	-38.51 ± 0.38	4.15 ± 0.35	18.66			

Notes. Primaries in this sample are from Tycho-Gaia astrometric solution catalog (TGAS; Michalik et al., 2015), and the secondaries are from SDSS DR12 sample in Anguiano et al. (2017).

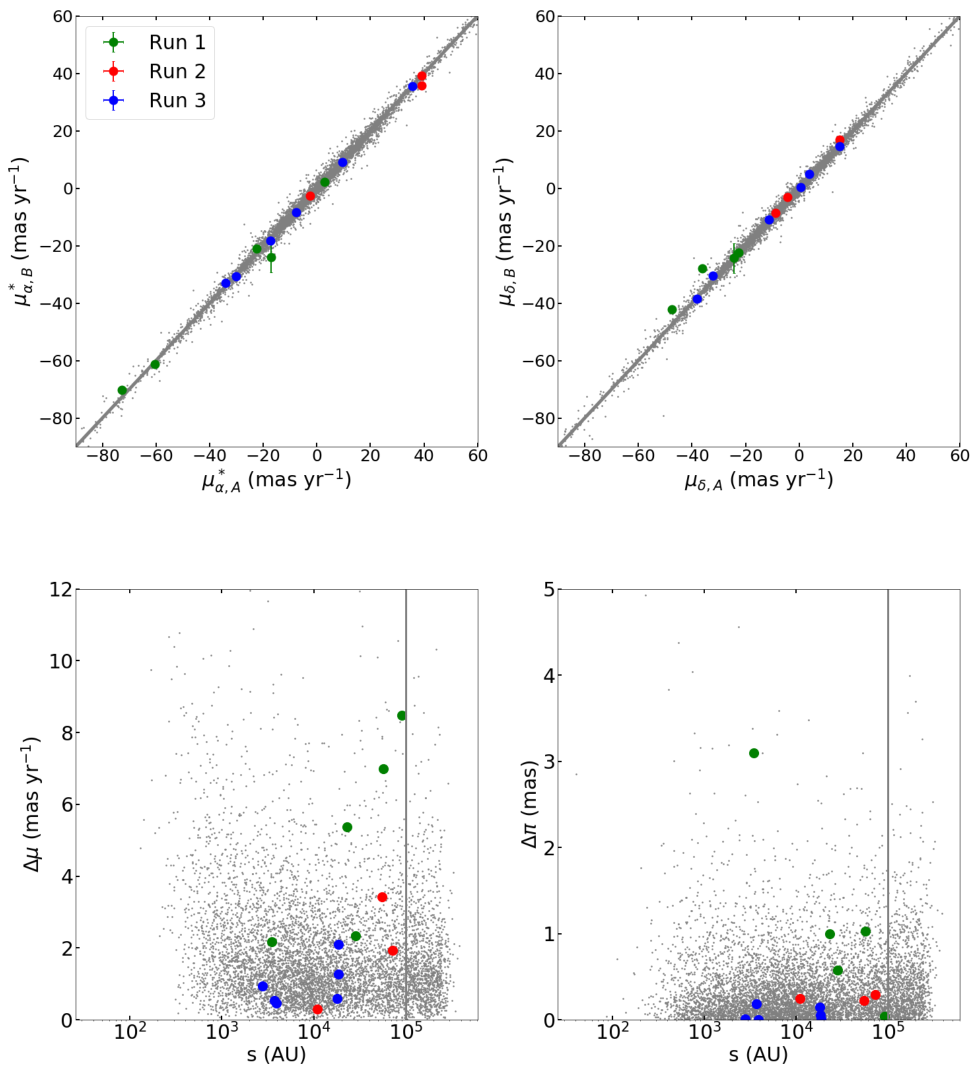

Figure 2.2: Top panel: Comparison of proper motion components, left panel shows right ascension (μ_α) and right panel declination (μ_δ). Bottom panel: Difference in proper motion and parallax for our WB sample in terms of projected separation, the grey line shows 10^5 AU limit. Green, red and blue dots are our sample of WBs observed, and the grey background is the WB catalog from Andrews et al. (2017).

2.2.3 Data Reduction

The spectra obtained in these three runs were reduced using the CarPy pipeline[1], which trims the image and corrects for overscan, applies the flat fields to the object images, removes scattered light and subtracts sky background. It proceeds to extract the stellar flux order-by-order, and it applies a wavelength mapping based on Th-Ar lamp exposures taken before each observed star. The S/N of our reduced spectra (per pixel) varies between 100 and 300 at $\lambda = 6000$ Å with a median S/N ~ 180. Continuum normalization of the spectra of each star order-by-order was done using common IRAF[2] task, and we measured the radial velocities using the standard cross-correlation function with a radial velocity standard of Soubiran et al. (2018). The accuracy of these values (~ 0.5 km s^{-1}) is sufficient for our purposes.

[1] `https://code.obs.carnegiescience.edu/mike`

[2] IRAF is the Image Reduction and Analysis Facility, a general-purpose software system for the reduction and analysis of astronomical data. IRAF is written and supported by National Optical Astronomy Observatories (NOAO) in Tucson, Arizona.

Chapter 3

Procedures and Results

3.1 Analysis of White Dwarfs

3.1.1 Effective Temperatures and Surface Gravities for White Dwarfs

Our sample of 14 WBs contains only DA WDs as secondaries. This type of WDs with hydrogen-rich atmospheres comprise ~ 85 percent of all WDs (see Kepler et al., 2019). The newest data obtained by the *Gaia* mission allow us to study this group of stars in more detail. Using accurate parallaxes, existing photometry and atmospheric models for WDs it is possible to determine stellar parameters (e.g. Kilic et al., 2019; Gentile Fusillo et al., 2019). On the other hand, there is the spectroscopic method that uses the WDs spectra. The observed line profiles contain a wealth of information about the effective temperature (T_{eff}) and surface gravity (log g). In particular, the profiles of all Balmer lines are quite sensitive to T_{eff} variations, as well as log g variations (Bergeron et al., 1992).

The determination of atmospheric and physical parameters for the DA WDs is usually accomplished by comparing predicted fluxes from model atmosphere calculations with spectroscopic data. The first step is to normalize the line flux, in both observed and model spectra, to a continuum set to unity at a fixed distance from the line center. The comparison with model spectra, which are convolved with a Gaussian instrumental profile, is then carried out in terms of these line shapes only. The calculation of χ^2 is carried out using the normalized line profiles as defined above. Finally, the values of $T_{\rm eff}$ and log g are obtained by minimizing χ^2, the value of σ is calculated from the rms deviation of the observed spectrum from the best-fit model spectrum. This is then propagated into the covariance matrix, from which the formal uncertainties of the fitted atmospheric parameters are obtained. The fitting technique and model details can be seen in Bergeron et al. (1992).

Anguiano et al. (2017) (hereafter BA17) reported atmospheric parameters via the spectroscopic method using SDSS WD spectra from DR12. It is important to mention that these spectra are in several cases rather noisy. This is because WDs are generally faint objects. Hence, the stellar parameters derived from their spectra often have large uncertainties. The signal-to-noise (S/N) values reported in BA17 are an average of the S/N in four continuum spectral ranges with different central wavelengths. WD model atmosphere spectra of Koester (2010) are used to estimate effective temperatures and surface gravities of WDs, for which the parametrization of convection follows the mixing length formalism ML2/$\alpha = 0.8$. The mixing length theory (MLT) describes the convective transport of energy in the stellar interior; different convective efficiencies change the MLT between ML1 or ML2 (Fontaine et al., 1981). In this case ML2/$\alpha = l/H_p$, where l is the mixing length and H_p is the pressure scale height (Koester, 2010); this is a free parameter of order unity that determines how far a fluid parcel travels before it dissolves into the background.

Table 3.1: White Dwarfs Atmospheric Parameters: Step-by-Step Procedures

	BA17	KL13	KE1516
Spectra	SDSS	SDSS	SDSS
S/N	4-band average	g-band	g-band
WD model	Koester 2010	Koster 2010	Koester 2010
ML2/α	0.8	0.6	0.6
$T_{\rm eff}$ and log(g)	Fitting Technique	Fitting Technique	Fitting Technique
Errors	Spectroscopic	Spectrophotometric	Spectrophotometric

Other references reported atmospheric parameters for the WDs in our sample, as is the case of Kleinman et al. (2013) and Kepler et al. (2015, 2016) (hereafter KL13 and KE1516). The steps to achieve the atmospheric parameters for each reference are shown in Table 3.1; as we can see, all of them are similar, except for the mixing length theory and the error determination, the former indicating a more efficient convective energy transport for BA17 than KL13 and KE1516. The S/N, $T_{\rm eff}$ and log g for all references can be found in Table 3.2.

Errors are considerably smaller for the latest references, this is something that will make an impact at the moment of determining masses and cooling times for WDs. Therefore, the errors reported in BA17, KL13, and KE1516 warrant a closer inspection. The errors in BA17 are derived from the spectroscopic method explained at the beginning of this section. On the other hand, in KL13 and KE1516, they used a spectrophotometric method to estimate the stellar parameters and errors. Briefly, this approach uses the spectra and colors of WDs to classify them into DA or DB and measure atmospheric parameters by fitting the observed spectra to a synthetic model spectral grid by χ^2 minimization. After this, they supplement the spectroscopic fitting with additional information from SDSS photometry. Each model is convolved with the SDSS filter curves to yield predicted colors, then they construct the χ^2 statistic for the difference between the observed colors and the predicted colors. Finally, they sum the spectroscopic and photometric χ^2 with equal weight yielding the $T_{\rm eff}$ and log g. During the fitting process, they discuss that some lack of accuracy and an underestimate of errors are expected, especially for high S/N spectra. They also mention that differences with other references are probably due to the fitting method used, this explains the difference in both determinations. For more details see Kleinman et al. (2004).

Looking at WD's $T_{\rm eff}$ in Figure 3.1 top panel, we notice that $T_{\rm eff}$ are similar and consistent within the errors in most of the cases, following the 1:1 relation and covering a large range in $T_{\rm eff}$ from $\approx$ 6000 to 20000 K. SDSS J154634.50 is the only one that lays outside of this line despite the good S/N reported in both cases. The bottom panel in Figure 3.1 shows WD's surface gravities (log g), we can see that the sample follows the 1:1 line given the error bars. Also, the values are concentrated between 7.75 and 8.50 approximately; SDSS J220850.53 is the one with the lowest S/N, the biggest difference between references, and the larger errors.

Table 3.2: Effective Temperatures and Surface Gravities of White Dwarfs in our Wide Binaries

WD N°	Object ID (SDSS)	S/N	$T_{\rm eff}$ (K)	log(g) (cm s^{-2})	Ref.
1	J012824.93-082254.1	29.51	6459 ± 57	7.72 ± 0.13	1
		26.70	6653 ± 31	7.83 ± 0.07	2
2	J123604.65+170819.2	10.91	9570 ± 157	8.36 ± 0.20	1
		10.86	9351 ± 78	8.36 ± 0.11	2
3	J154634.50+233438.0	43.24	12182 ± 136	8.15 ± 0.04	1
		35.00	16673 ± 19	7.98 ± 0.02	3
4	J225247.41+270433.7	37.00	18542 ± 202	7.90 ± 0.04	1
		33.00	17786 ± 101	7.93 ± 0.02	3
5	J220850.53+001349.0	4.56	19416 ± 2294	7.68 ± 0.45	1
		4.46	18287 ± 776	8.07 ± 0.19	2
6	J001624.09+082157.0	26.39	16717 ± 304	7.85 ± 0.08	1
		24.00	16451 ± 20	7.94 ± 0.01	3
7	J021134.67-000025.9	11.92	10513 ± 222	8.16 ± 0.21	1
		11.24	10588 ± 102	8.38 ± 0.01	2
8	J211928.44-002632.9	6.06	17707 ± 1041	8.00 ± 0.23	1
		7.80	16454 ± 478	7.91 ± 0.10	2
9	J092228.57+121125.8	19.69	15782 ± 368	7.98 ± 0.08	1
		18.00	16143 ± 170	8.19 ± 0.03	2
10	J075019.11+181356.9	30.11	9166 ± 29	8.17 ± 0.07	1
		26.46	9175 ± 32	8.35 ± 0.04	2
11	J034315.83-060006.2	40.86	16149 ± 177	7.85 ± 0.05	1
		36.22	15949 ± 116	7.91 ± 0.02	2
12	J133619.70-025445.2	19.00	13019 ± 371	8.23 ± 0.11	1
		16.91	13218 ± 215	8.30 ± 0.07	2
13	J104959.79-004719.1	47.03	15601 ± 116	7.91 ± 0.03	1
		44.98	15422 ± 90	7.94 ± 0.02	2
14	J115357.30+190606.9	15.31	11883 ± 407	8.24 ± 0.14	1
		13.80	11909 ± 1309	8.02 ± 0.21	2

References. **1:** Anguiano et al. (2017) ; **2:** Kleinman et al. (2013) ; **3:** Kepler et al. (2015, 2016).

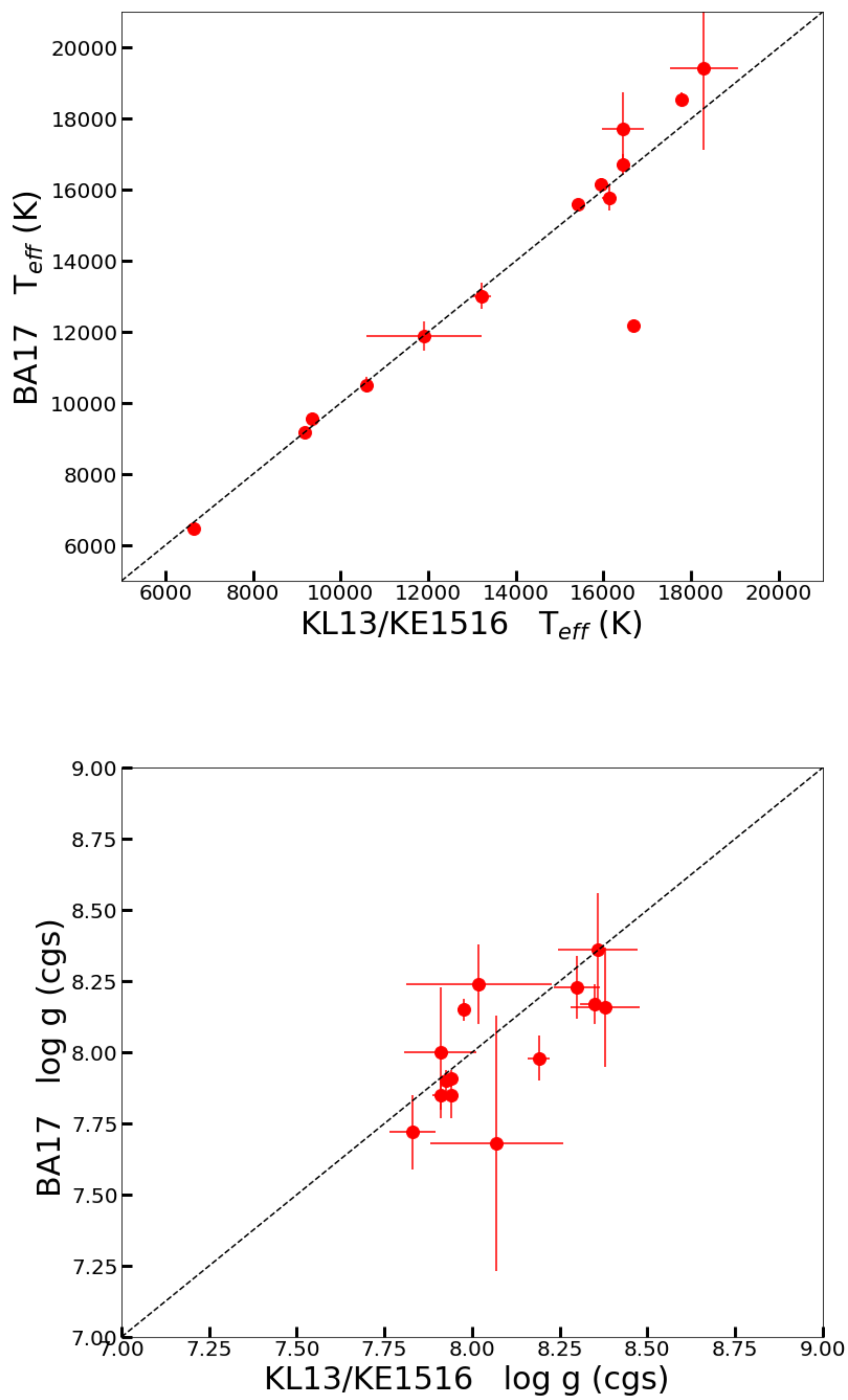

Figure 3.1: Effective temperatures (top panel) and surface gravities (bottom panel) comparison. References used were KL13 (Kleinman et al., 2013), KE1516 (Kepler et al., 2015, 2016) and BA17 (Anguiano et al., 2017).

3.1.2 Masses and Cooling Times for White Dwarfs

Masses and cooling times in BA17 were found interpolating T_{eff} and log g into cooling tracks from Althaus et al. (2010) and Renedo et al. (2010). KL13 and KE1516 masses were also obtained using the cooling tracks from Renedo et al. (2010) and Romero et al. (2015), but cooling times were not reported in the catalog. Consequently, we calculated cooling times and masses ourselves using evolutionary models. We did this interpolating the stellar parameters reported in KL13 and KE1516 into cooling tracks from Fontaine et al. (2001) (hereafter F01) available in the Montreal White Dwarfs Database (hereafter MWDD) [1] (Dufour et al., 2017). To use the models, it is necessary to set up the spectral type and envelope thickness, here we selected "DA" and "thick", respectively. F01 mentions that DA WDs can be represented by DA models with this type of envelope. To check the masses obtained in this work, we compared them with KL13 and KE1516 reported masses, this can be seen in Fig. 3.2, where it is clear that both results follow the 1:1 relation, and our determination of masses is reliable.

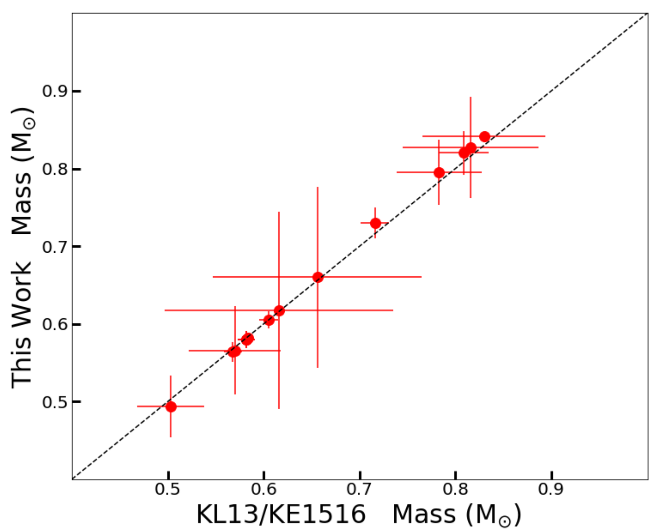

Figure 3.2: Comparison between masses reported in KL13/KE1516 using cooling tracks of Renedo et al. (2010) and Romero et al. (2015), and masses obtained in this work using KL13/K1516 atmospheric parameters interpolated into cooling tracks from Fontaine et al. (2001).

[1] http://www.montrealwhitedwarfdatabase.org/

A comparison between masses and cooling times from this work with the measurements from BA17 can be seen in Table 3.3 and in Figure 3.3. Looking at both parameters, there is not a tendency or systematic error in favor of any of the references, and all the points are distributed along the 1:1 line. For the masses, there is just one WD with a relative difference of 25.8%, five WDs between 10 and 20% and eight WDs under 10%. The biggest difference is ≈ 0.17 $M_{\odot}$ for SDSS J220850.53+001349.0, but this WD mass also has an error about 50% of the estimated value in BA17. Overall, WDs mass measurements are consistent within the errors, except for SDSS J154634.50, SDSS J092228.57 and SDSS J075019.11. For cooling times, SDSS J154634.50 has a relative difference of 72.9% between measurements. There are also four WDs cooling times with relative differences between 20 and 35%, and eight WDs under 10% difference. For short cooling times, small variations can be relevant at the moment of determining initial masses, we will see this in Section 3.3. We can expect a certain scatter in the masses and cooling times measurements given the different sets of atmospheric parameters used, and also because we are using a different set of cooling tracks.

Overall, KL13 and KE1516 obtained more precise parameters than BA17 in both effective temperature and surface gravities. These lead to better masses and cooling times determinations. For our purposes, we need the best precision to constrain the IFMR, but in this case, we cannot select one set of parameters and reject the other. The reason is that we have 2 different error determinations, both equally valid. Hence, we will use both sets of atmospheric parameters and determine later what is the impact, if any, on the constraints for the IFMR.

Table 3.3: Masses and Cooling Times of White Dwarfs in our Wide Binaries

WD N°	Object ID (SDSS)	M_{WD} ($M_\odot$)	τ_{cool} (Gyr)	Ref.
1	J012824.93-082254.1	0.456 ± 0.070	$1.97^{+0.04}_{-0.04}$	1
		0.494 ± 0.040	$1.36^{+0.15}_{-0.13}$	2
2	J123604.65+170819.2	0.819 ± 0.110	$1.30^{+0.52}_{-0.40}$	1
		0.827 ± 0.065	$1.28^{+0.40}_{-0.25}$	2
3	J154634.50+233438.0	0.696 ± 0.029	$0.48^{+0.03}_{-0.03}$	1
		0.605 ± 0.011	$0.13^{+0.01}_{-0.01}$	2
4	J225247.41+270433.7	0.572 ± 0.023	$0.09^{+0.01}_{-0.01}$	1
		0.580 ± 0.011	$0.10^{+0.01}_{-0.01}$	2
5	J220850.53+001349.0	0.486 ± 0.239	$0.07^{+0.04}_{-0.02}$	1
		0.660 ± 0.116	$0.11^{+0.07}_{-0.05}$	2
6	J001624.09+082157.0	0.544 ± 0.040	$0.13^{+0.01}_{-0.01}$	1
		0.582 ± 0.001	$0.13^{+0.01}_{-0.01}$	2
7	J021134.67-000025.9	0.696 ± 0.129	$0.71^{+0.16}_{-0.28}$	1
		0.842 ± 0.006	$0.91^{+0.04}_{-0.04}$	2
8	J211928.44-002632.9	0.618 ± 0.148	$0.12^{+0.02}_{-0.06}$	1
		0.566 ± 0.057	$0.12^{+0.04}_{-0.03}$	2
9	J092228.57+121125.8	0.603 ± 0.060	$0.17^{+0.03}_{-0.01}$	1
		0.730 ± 0.020	$0.22^{+0.02}_{-0.02}$	2
10	J075019.11+181356.9	0.698 ± 0.042	$1.01^{+0.11}_{-0.09}$	1
		0.820 ± 0.028	$1.32^{+0.16}_{-0.13}$	2
11	J034315.83-060006.2	0.542 ± 0.027	$0.15^{+0.01}_{-0.01}$	1
		0.564 ± 0.013	$0.14^{+0.01}_{-0.01}$	2
12	J133619.70-025445.2	0.738 ± 0.070	$0.45^{+0.09}_{-0.08}$	1
		0.795 ± 0.042	$0.45^{+0.07}_{-0.06}$	2
13	J104959.79-004719.1	0.569 ± 0.026	$0.17^{+0.01}_{-0.01}$	1
		0.580 ± 0.011	$0.16^{+0.01}_{-0.01}$	2
14	J115357.30+190606.9	0.740 ± 0.089	$0.58^{+0.15}_{-0.12}$	1
		0.617 ± 0.127	$0.39^{+0.34}_{-0.17}$	2

References. 1: Anguiano et al. (2017) ; **2:** Masses and cooling from evolutionary models of Fontaine et al. (2001).

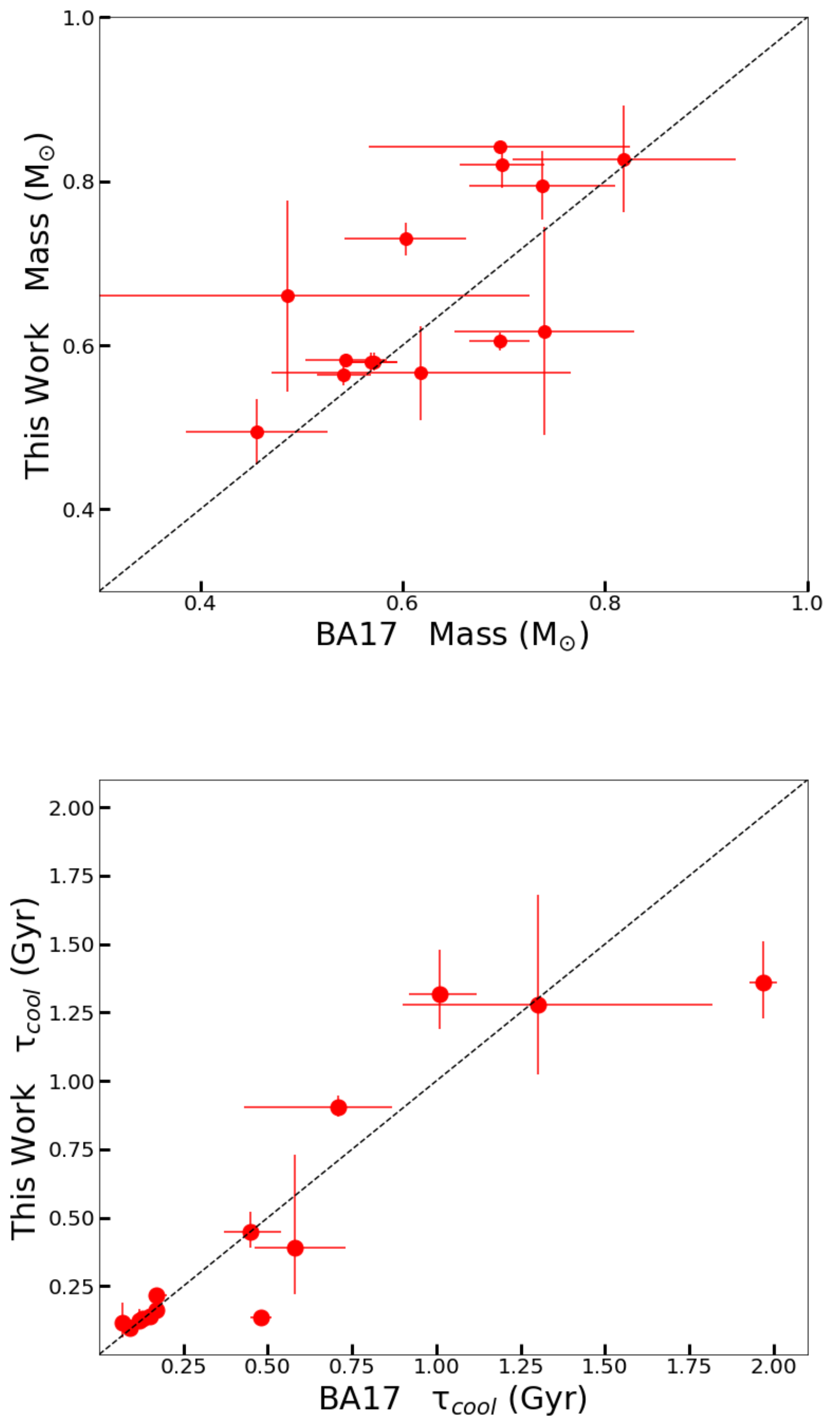

Figure 3.3: Masses (top panel) and cooling times (bottom panel) comparison between the results in this work using Fontaine et al. (2001) cooling tracks and BA17 (Anguiano et al., 2017) using Renedo et al. (2010) cooling tracks.

3.2 Analysis Turnoff/Subgiant

3.2.1 Determination of Atmospheric Parameters

The fundamental atmospheric parameters T_{eff}, log g, and [Fe/H][2] of a star can be estimated using a variety of techniques (e.g., Barklem et al., 2002; Ramírez et al., 2006, 2013; Ramírez et al., 2014; Chanamé and Ramírez, 2012). In addition to employing only the observed spectra, photometric data, as well as trigonometric parallaxes can be used to constrain one or more of these quantities. In our work, we use the spectroscopic approach, which measures iron abundances (Fe I and Fe II) in the star's atmospheres. This is the main ingredient to determine atmospheric parameters (Ramírez et al., 2014). To calculate these values we used the curve-of-growth method, and the analysis was made using the spectrum synthesis code MOOG[3] (Sneden, 1973). The atmospheric models adopted are from the MARCS grid of 1D-LTE standard chemical composition (Gustafsson et al., 2008).

We used a set of 99 iron lines from Asplund et al. (2009) selected for our type of stars, where 74 are Fe I lines and 15 are Fe II. Each one of these lines has atomic data measured: the excitation potential (EP=χ) and transition probability (log (gf)). Most of our iron lines are completely unblended. However, our Fe I linelist includes a few lines that are somewhat affected by other nearby spectral features. The reason to keep these lines is to avoid degeneracies and biases in the determination of stellar parameters using the standard excitation/ionization balance technique which is described in the next paragraphs. In addition to retaining as many as possible low-χ lines, even if they are difficult to measure, we had to exclude a number of very good (i.e., clean) lines on the high-χ side, also to prevent biasing the atmospheric parameter determination. Having an unbalanced χ distribution would make the T_{eff} more sensitive to one particular type of spectral line, which should be avoided.

We measured the equivalent width (EW) of these iron lines one-by-one for each star in our sample "manually" using IRAF's task splot. Gaussian fits were preferred to reduce the impact of observational noise on the lines' wings. At the spectral resolution of our data, Gaussian fits are acceptable. We also made sure to adopt

[2] We use the standard notation: $[\mathrm{Fe/H}] = A_{\mathrm{Fe}} - A^{\odot}_{\mathrm{Fe}}$, where $A_{\mathrm{Fe}} = \log(N_{\mathrm{Fe}}/N_{\mathrm{H}}) + 12$ and N_x is the number density of X atoms in the stellar photosphere

[3] http://www.as.utexas.edu/~chris/moog.html

consistent pseudo-continua for all stars. We compared our manual measurements of EWs with automated procedures such as DAOSPEC (Stetson and Pancino, 2008), both of them yielded similar values, but in terms of achieving consistency and accuracy, we preferred to use the former. Although these automated procedures are extremely helpful when dealing with very large numbers of stars and long spectral line-lists, which is not our case. An extraction of the iron linelist and the EWs measured for one of our sample stars is shown in Table 3.4 as an example.

Table 3.4: Iron linelist extraction for TYC 5274-489-1

Wavelength (Å)	Species	χ (eV)	log (gf)	$EW_{\odot}$ (mÅ)	EW_{star} (mÅ)
4994.129	26.000	0.915	-3.080	102.0	99.3
5198.710	26.000	2.220	-2.140	99.2	94.1
5225.525	26.000	0.110	-4.789	74.9	66.0
5242.490	26.000	3.630	-0.990	87.7	85.4
.	.	.	.	.	.
.	.	.	.	.	.
.	.	.	.	.	.
6084.090	26.100	3.200	-3.830	21.1	33.3
6149.240	26.100	3.890	-2.750	36.2	56.4
6369.462	26.100	2.891	-4.110	19.7	29.6
6432.676	26.100	2.891	-3.570	42.4	59.1
6456.383	26.100	3.904	-2.050	65.3	87.2

Notes. The $EW_{\odot}$ are measured using a solar spectrum as reference, which is based on spectra of sunlight reflected from asteroids, Hebe in this case. The EW_{star} corresponds to TYC 5274-489-1.

We employed the excitation/ionization balance technique to find the atmospheric parameters that produce consistent iron abundances. A first guess of the atmospheric parameters T_{eff}, log g, [Fe/H], v_t is made, and these are iteratively modified until the correlations between iron abundance and χ of Fe I lines were minimized (forcing excitation balance), while simultaneously minimizing the difference between the mean iron abundances derived from Fe I and Fe II (achieving ionization balance). The correlation between Fe I abundance and the line strength is controlled (i.e., the correlation is minimized) with the microturbulent velocity parameter v_t. To simplify the manipulation of MOOG's input and output as well as the iterative procedures, we used q^2 Python package[4].

We used a strict differential approach for the calculations described here. This means that the stars' iron abundances were measured relative to the solar iron abundance on a line-by-line basis, the latter was inferred from a solar spectrum as reference, which is based on spectra of sunlight reflected from asteroids, Hebe in this case. Thus, if $A_{\mathrm{Fe,i}}$ is the absolute iron abundance derived for a spectral line i, the final relative iron abundance [Fe/H] is the average of $A_{\mathrm{Fe,i}}$ - $A^{\odot}_{\mathrm{Fe,i}}$ for each line measured. Strict differential analysis minimizes the impact of model uncertainties as well as errors in atomic data because they cancel-out in each line calculation.

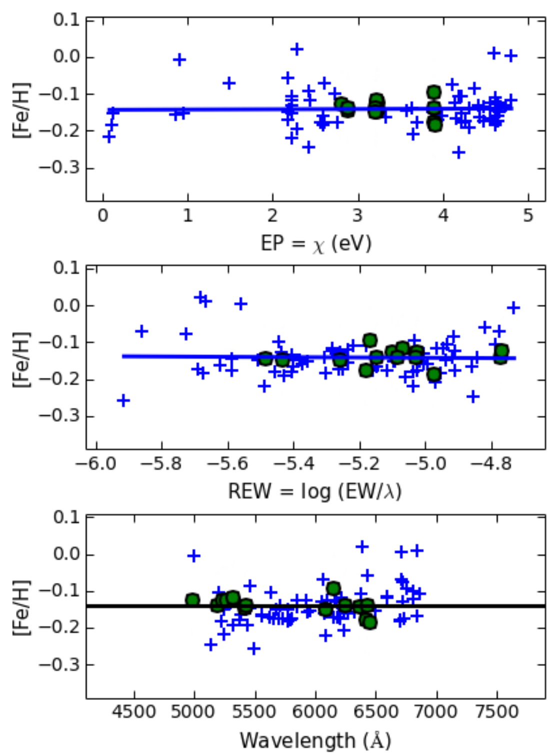

Figure 3.4: Line-to-line relative iron abundance of TYC 5274-489-1 as a function of excitation potential (top panel), reduced equivalent width (middle panel), and wavelength (bottom panel). Crosses (circles) are Fe I (Fe II) lines. The solid lines in the top and middle panels are linear fits to the Fe I data. In the bottom panel, the solid line is a constant which corresponds to the average iron abundance

[4] q^2 is a Python package developed by Ivan Ramirez. The q^2 source code is available online at `https://github.com/astroChasqui/q2`

In each iteration, the slopes of the [Fe/H] vs. χ and [Fe/H] vs. REW (which is defined as REW = log(EW/λ); with λ equals the wavelength of the line) relations were examined. If they were found positive (negative), the $T_{\rm eff}$ and v_t values were increased (decreased). At the same time, if the mean Fe I minus Fe II iron abundance difference was found positive (negative), the log g value was increased (decreased). We stopped iterating when the standard deviations of the parameters from the last five iterations were all lower than 0.8 times the size of the variation step. The first set of iterations was done with relatively large steps; the $T_{\rm eff}$, log g, and v_t parameters were modified by $\pm$32 K, $\pm$0.32, and $\pm$0.32 km s^{-1}, respectively. After the first convergence, the steps were reduced in half, i.e., to $\pm$16 K, $\pm$0.16, and $\pm$0.16 km s^{-1}, and so on, until the last iteration block, in which the steps were $\pm$1 K, $\pm$0.01, and $\pm$0.01 km s^{-1}. An example of this procedure end product is shown in Fig. 3.4 for one of the stars in our sample.

Errors in the derived parameters are estimated from the uncertainty in the abundance vs. χ slope (for $T_{\rm eff}$) and the line-to-line scatter of the mean Fe I and Fe II abundances (for log g). Since we force the χ slope to be zero, a slightly positive (negative) χ slope implies a $T_{\rm eff}$ too low (high) by a certain amount. We use the Δ $T_{\rm eff}$ amount that corresponds to a χ slope of $\pm 1\sigma$, where σ is the error of the zero slope when using the adopted $T_{\rm eff}$. For the error in log g, we consider the maximum and minimum log g values such that the mean (Fe I - Fe II) abundance difference is consistent with zero within the 1σ line-to-line scatter as the upper and lower limits of the derived log g. For [Fe/H], the formal error was computed by propagating the errors in the other atmospheric parameters into the [Fe/H] calculation; adding them in quadrature (therefore assuming optimistically that they are uncorrelated) and including the standard error of the mean line-to-line [Fe/H] abundance. It is important to mention that the errors obtained in this procedure correspond to the precision with which we are able to minimize the slopes and iron abundance difference. Rarely do they represent the true errors of the atmospheric parameters because they are instead largely dominated by systematic uncertainties (see Ramírez et al., 2014).

The complete set of atmospheric parameters for the primaries in our sample are in Table 3.5. The range in $T_{\rm eff}$ goes from 4849 to 6668 K, with internal uncertainties better than 2%. For log g the values are between 4.45 and 2.50 cm s^{-2}, but most of our sample is focused between 4.20 and 3.34 cm s^{-2}, the errors are under 0.1 in most cases. And [Fe/H] oscillate between -0.5 and 0.5 dex, with an average error of 0.02. In our sample, despite the high S/N of TYC 4969-457-1, MOOG could not find convergence during the iteration process, this is because the spectra showed readout problems during the observing night. Therefore, we will not use this pair to constrain the IFMR. As a check test, we compared our atmospheric parameters with the literature (See Appendix A).

Table 3.5: Atmospheric Parameters for the Observed Primary Stars in our Wide Binaries

SG N°	Object ID (TYC)	S/N	V (mag)	T_{eff} (K)	log g (cm s^{-2})	[Fe/H] (dex)	v_t (km s^{-1})
1	5274-489-1	100	9.24	6009 ± 32	4.20 ± 0.06	-0.14 ± 0.02	1.19 ± 0.05
2	1446-1524-1	223	9.43	5958 ± 28	3.95 ± 0.08	-0.53 ± 0.02	1.20 ± 0.07
3	2033-5-1	111	11.21	6179 ± 32	4.22 ± 0.07	0.23 ± 0.03	1.24 ± 0.05
4	2229-1088-1	258	9.54	5151 ± 24	3.34 ± 0.08	-0.22 ± 0.02	1.29 ± 0.05
5	558-2215-1	317	9.60	4849 ± 48	2.50 ± 0.16	-0.22 ± 0.04	1.58 ± 0.06
6	595-764-1	123	9.48	6564 ± 83	3.90 ± 0.15	-0.08 ± 0.05	1.55 ± 0.14
7	38-358-1	101	11.43	5723 ± 29	4.11 ± 0.06	-0.22 ± 0.02	1.14 ± 0.05
8	5194-1015-1	127	11.00	6353 ± 46	3.99 ± 0.09	-0.27 ± 0.03	1.44 ± 0.10
9	823-447-1	79	12.00	6668 ± 131	4.53 ± 0.22	0.11 ± 0.08	2.39 ± 0.28
10	1366-1363-1	185	9.04	6408 ± 64	4.01 ± 0.10	0.06 ± 0.04	1.68 ± 0.08
11	4723-595-1	166	12.22	5880 ± 19	4.45 ± 0.06	-0.31 ± 0.02	1.23 ± 0.05
12	4969-457-1	369	8.61	-	-	-	-
13	4913-1024-1	216	10.12	5798 ± 23	4.19 ± 0.04	0.49 ± 0.02	1.19 ± 0.04
14	1443-1882-1	147	10.71	5281 ± 19	3.88 ± 0.05	-0.04 ± 0.02	1.04 ± 0.04

Notes. For TYC 4969-457-1, MOOG could not find convergence during the iteration process.

3.2.2 Age Determination

The determination of stellar ages is usually subject to a series of inaccuracies and biases. In particular, if we consider systems in which the stars are in the MS, using a method such as the one of isochrones makes them even worse because most of these theoretical curves have similar trajectories within this evolutionary stage. On the other hand, for recently evolved stars in the turnoff or subgiant branch, isochrone fitting technique can give us precise ages due to the clear separation that exists between the different theoretical curves, a reflection of the rapid evolution along these phases in comparison to the MS.

For our sample of WBs, we developed a code that computes the ages using this technique. The primary star under study is placed on a HR diagram and its location compared to theoretical predictions of stellar evolution. Isochrone points close to the observed stellar parameters are then used to derive the age of the star (e.g., Lachaume et al., 1999; Nordström et al., 2004; Jørgensen and Lindegren, 2005; Chanamé and Ramírez, 2012). While the location of any star on the HR diagram is determined just by its absolute luminosity Mv (or log g) and surface temperature $T_{\rm eff}$ (or color), we also need the metallicity value to avoid possible degeneration effects in the age determination (see da Silva et al., 2006; Jørgensen and Lindegren, 2005) of a star. The fundamental atmospheric parameters are measured from the star's spectrum as we did in Section 3.2.2. It is possible to use the surface gravity log g instead of the absolute magnitude Mv, but given that we have exquisite parallaxes measured by *Gaia* (Gaia Collaboration et al., 2018), we decided to use the absolute magnitude of the star which is determined by its apparent magnitude and parallax.

To determine which isochrone best fits any particular star, we built the probability distribution function (hereafter PDF) of the stellar age by computing the likelihood that any given isochrone passes near the corresponding set of stellar parameters, accounting for the uncertainties on those parameters. The age PDF is also called the "G-function", and the procedure is widely used nowadays (e.g., Allende Prieto et al., 2004; Nordström et al., 2004; Jørgensen and Lindegren, 2005; Chanamé and Ramírez, 2012). Assuming that the errors in our stellar parameters ($\sigma_{T_{\rm eff}}$, $\sigma_{\rm [Fe/H]}$ and $\sigma_{\rm Mv}$) have Gaussian probability distributions, the likelihood for a point in a given isochrone can be written as

$$P(T_{\rm eff}, {\rm [Fe/H]}, M_{\rm v}) \propto \exp\left[\frac{-(\Delta \log T_{\rm eff})^2}{2\sigma^2_{\log T_{\rm eff}}}\right] \exp\left[\frac{-(\Delta{\rm [Fe/H]})^2}{2\sigma^2_{\rm [Fe/H]}}\right] \times \exp\left[\frac{-(\Delta M_{\rm v})^2}{2\sigma^2_{M_{\rm v}}}\right], \tag{3.1}$$

where $\Delta \log T_{\rm eff}$, Δ[Fe/H], and $\Delta M_{\rm v}$ are the differences between the measured stellar parameters and those corresponding to the point in the isochrone under consideration. The integral of this likelihood over all the parameter space of the set of isochrones then gives the age probability distribution

$$P(Age) = \int P(\log T_{\rm eff}, {\rm [Fe/H]}, M_{\rm v}) {\rm d} \log {\rm T_{eff}} {\rm d[Fe/H]} {\rm dM_v}. \tag{3.2}$$

In practice, we only integrate over the volume defined by three times the 1σ uncertainties from the measured stellar parameters, which we verified already accounts for most of the contribution to the PDF from the entire set of isochrones. We also normalized the distributions so that the area below is equal to 1. Then, we adopted the peak of the G-function as the most likely age of the star. The adopted errors (dashed lines) are computed using the cumulative function of the age PDF, assuming that the latter is well approximated by a Gaussian. However, this G-function is not always close to a Gaussian, and thus we adopt different 1σ errors to both sides of the peak. Our 1σ lower and upper limits mark the age interval of cumulative probability between 16% and 84%. Using this procedure, we computed the ages of all primaries in our sample. We used Yale-Yonsei isochrones (hereafter $\texttt{Y}^2$) (Yi et al., 2001; Demarque et al., 2004) sampled with constant steps of 0.1 Gyr in age and 0.02 dex in [Fe/H], covering ages from 0.1 to 15 Gyr and [Fe/H] from -1.72 to 0.6 dex. This isochrone grid has a very fine spacing in metallicity, which allows us to determine with more precision the shapes of the age probability distributions without having to increase arbitrarily the error bar in [Fe/H], as it is sometimes done. The latter could introduce biases in the age determination scheme (Ramírez et al., 2013). In constructing the age PDF, we experimented with different bin sizes and found that 0.2 Gyr/bin was an optimal choice. Smaller bin sizes yield similar ages (see Appendix B).

Besides, we tested `PARSEC` isochrones by Bressan et al. (2012) to compare the ages obtained using a different set of isochrones. We used the web interface PARAM 1.3[5] (da Silva et al., 2006). This tool uses a slightly modified version of the Bayesian estimation method by Jørgensen and Lindegren (2005). The Bayesian method builds a complete PDF separately for each stellar property under study (e.g, age), taking as input the effective temperature, metallicity, and absolute magnitude of a star; also Bayesian priors as the initial mass function and a constant star formation rate. Briefly, considering a small section of an isochrone of metallicity [Fe/H]$'$ and age t$'$, corresponding to an interval of initial masses [$\mathrm{M_i^1}$, $\mathrm{M_i^2}$] and with mean properties, $\mathrm{M_v'}$, $\mathrm{T_{eff}'}$, the probability of the observed star to belong to this section is computed as follows

$$P^{12}(t') \propto \int_{M_\mathrm{i}^1}^{M_\mathrm{i}^2} \phi(M_\mathrm{i}) dM_\mathrm{i} \exp\left[-\frac{(\log T_\mathrm{eff} - \log T_\mathrm{eff}')^2}{\sigma^2_{\log T_\mathrm{eff}}} - \frac{(M_\mathrm{v} - M_\mathrm{v}')^2}{\sigma^2_{M_\mathrm{v}}}\right], \qquad (3.3)$$

where the first term represents the relative number of stars populating the [M_i^1, M_i^2] interval according to the initial mass function ϕ(Mi), and the second term represents the probability that the observed $\mathrm{M_v}$ and $\mathrm{T_{eff}}$ correspond to the theoretical values, for the case that the observational errors have Gaussian distributions. Then, summing over $\mathrm{P}^{12}(t')$ the cumulative histogram of P(t) is obtained. For more details see da Silva et al. (2006).

The resulting ages and uncertainties for all the primaries in our sample are listed in Table 3.6, for both theoretical isochrones, $\mathtt{Y}^2$ and `PARSEC`. Primary stars marked with * are out of the ideal evolutionary stage (TO or SG), and for stars marked with **, the age PDF could not be calculated for one of the isochrone sets. In the case of TYC 4723-595-1, which is a clear MS star with log(g)= 4.45 (Sun's log(g) $\sim$ 4.40) and also for TYC 823-447-1 with big uncertainties in the atmospheric parameters, the age determination is bad and our program can not fit isochrones to these stars precisely. We can see the age PDFs in the left panel of Fig. 3.5 and Fig. 3.6 using Y^2 isochrones; the right panel shows the HR diagram with the isochrone fitted to the primary star for a given metallicity. The blue PDFs and blue dots in the HR diagram represent those stars that are not considered TO or SG.

[5] `http://stev.oapd.inaf.it/cgi-bin/param_1.3`

Table 3.6: Ages for Primaries in Our Wide Binary Sample

Object ID (TYC)	Age Y^2 (Gyr)	Age PARSEC (Gyr)
5274-489-1*	$5.61^{+0.60}_{-0.64}$	6.72 ± 0.61
1446-1524-1	$5.41^{+0.18}_{-0.15}$	5.94 ± 0.18
2033-5-1*	$2.21^{+0.23}_{-0.76}$	1.72 ± 0.46
2229-1088-1	$2.00^{+0.07}_{-0.12}$	2.18 ± 0.10
558-2215-1*	$1.40^{+0.46}_{-0.20}$	2.23 ± 0.84
595-764-1	$1.80^{+0.15}_{-0.08}$	1.89 ± 0.09
38-358-1	$11.20^{+0.31}_{-0.89}$	11.41 ± 0.19
5194-1015-1	$3.58^{+0.04}_{-0.68}$	3.17 ± 0.35
1366-1363-1	$2.40^{+0.24}_{-0.09}$	2.29 ± 0.24
1443-1882-1	$6.80^{+0.79}_{-0.58}$	7.13 ± 0.33
4913-1024-1	$3.60^{+0.16}_{-0.10}$	3.44 ± 0.12
4727-595-1**	0.10 ± 0.82	-
823-447-1**	-	0.30 ± 0.19

Notes. *: Primary stars out of the ideal evolutionary stage.
**: Primary stars with only one age determination.

Looking at the comparison of ages in Fig 3.7, we see consistency within the errors. Our sample follows the 1:1 relation, and there is not a systematic offset for the ages. The relative differences between the ages are under 12% for most of the stars but TYC 5274-489-1, TYC 2033-5-1, and TYC 558-2215-1 with differences of 18%, 25%, and 45% respectively (blue dots in Fig 3.7). Considering that these three primaries are out of the TO or SG zone (see right panel of Fig. 3.5, 3.6), we can expect a certain offset between models. Also, TYC 2033-5-1 and TYC 558-2215-1 have uncertainties

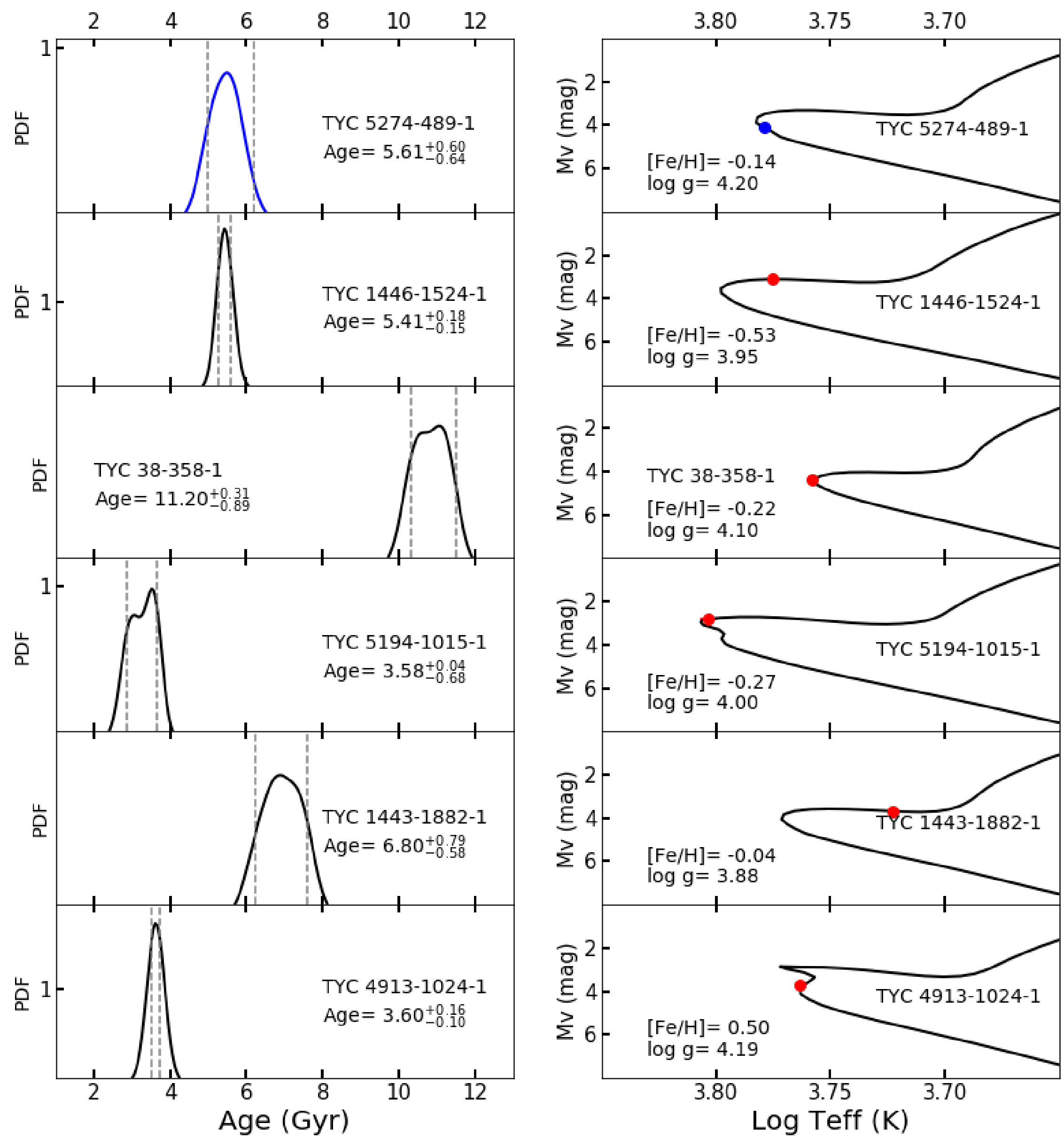

Figure 3.5: Left panel: Age PDF for each primary in our sample. The peak of the distribution is the most probable age for a star, and grey dotted line shows the upper (84 %) and lower (16%) 1σ error. Right panel: Isochrone of the most probable age fitted to the primary star (red/blue dot) using star metallicity, also surface gravity value is shown. Blue PDFs and blue dots indicate those stars outside of the ideal evolutionary stage.

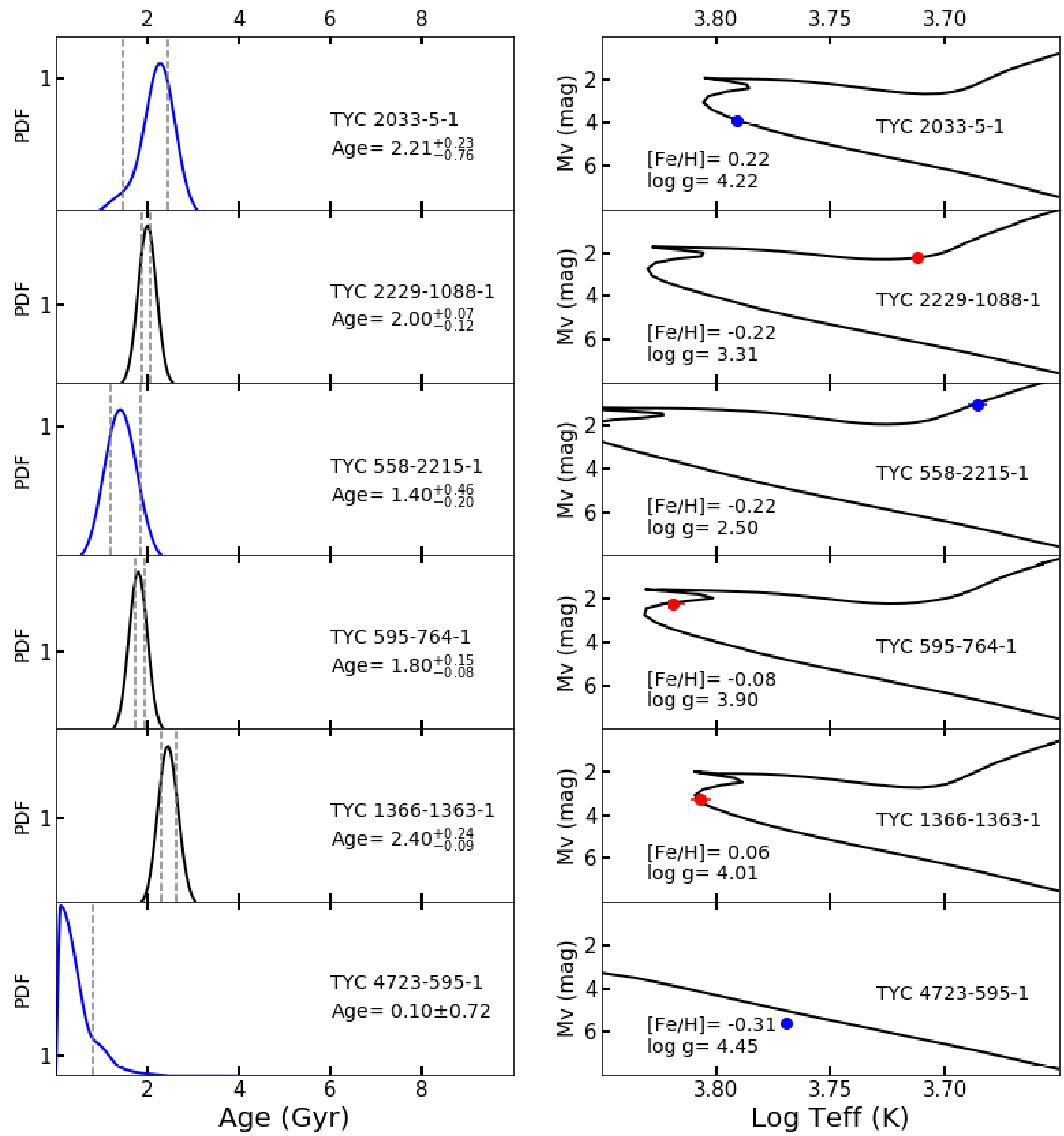

Figure 3.6: Continuation of Figure 3.5

corresponding to 34% and 33% of the value obtained, respectively. Moreover, TYC 5194-1015-1 has an error of 18%, and the other ages measured have errors under 12%.

Overall, our ages show consistency for different methods and isochrones. We have also shown that it is possible to achieve an precision better than 12% for TO and SG stars. Considering the results obtained in this section, we will not use the 2 pairs containing TYC 4723-595-1 and TYC 823-447-1 to constrain the IFMR, because there was not a clear age determination for these two primaries, reducing our useful sample to 11 WBs. On the other hand, the stars outside of the TO or SG phase (TYC 5274-489-1, TYC 2033-5-1 and TYC 558-2215-1) will be treated differently, and we will show in Chapter 4 the constraints found with these pairs in blue.

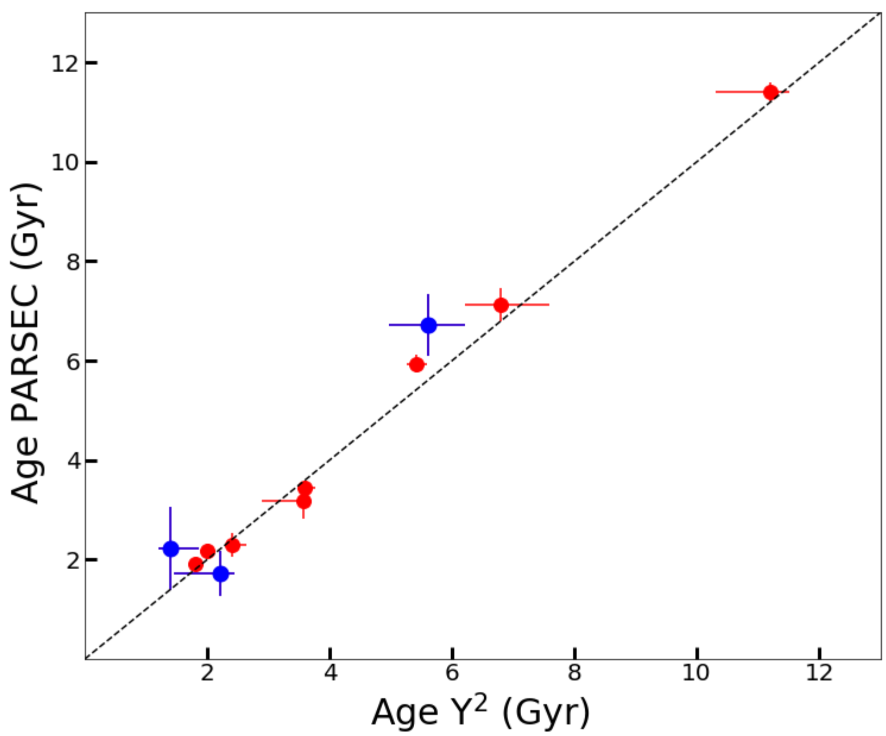

Figure 3.7: Comparison of ages using `Y`^{2} isochrones (Yi et al., 2001) and `PARSEC` isochrones (Bressan et al., 2012). Blue dots show stars out of the ideal evolutionary stage.

3.3 Initial Mass Determination and IFMR

Once we have the age of the system (i.e, the TO/SG age), the final step to constrain the IFMR is to calculate the progenitor's lifetime for each WD in our pairs, and with these values infer the initial masses using stellar evolution models. The progenitor's lifetime (τ_{prog}) is obtained using Equation 1.4, subtracting the cooling time (τ_{cool}) determined in Section 3.1 to the TO/SG age ($\mathrm{Age}_{\mathrm{SG}}$) obtained in the previous section. We assumed that both stars TO/SG and WD are co-eval. Considering the arguments exposed at the beginning of this thesis (see Section 1.2.2), and the fact that our sample is formed by old enough pairs, the small difference in age between the two components due to any age spread of their original formation site is negligible.

The next step is to build a progenitor lifetime function (hereafter PLF) using stellar evolution models. This function allows us to track each progenitor lifetime into an initial mass for a given metallicity (see Fig. 3.8). We used the MESA Isochrones and Stellar Tracks (`MIST`; Dotter, 2016; Choi et al., 2016) to do this. The `MIST`[6] stellar evolutionary tracks are computed with the Modules for Experiments in Stellar Astrophysics (`MESA`; Paxton et al., 2011, 2013, 2015) code. `MESA`[7] is an open-source stellar evolution package that includes integrated equations-of-state tables, opacity tables, nuclear reaction networks, and elemental diffusion rates. The `MIST` project produces extensive grids of stellar evolutionary tracks and isochrones that cover a wide range in stellar masses from 0.1 to 300 $M_\odot$ and metallicities from -2.0 to +0.5 dex. The latter is one of the main reasons to use these models, the wide extension and fine grid (0.01 dex), help us to estimate good initial masses. The physics adopted in the models and their implementation in `MESA` is explained in Choi et al. (2016).

In terms of consistency, we chose to use `MIST` evolutionary tracks because `Y`^{2} tracks can reproduce the evolution up to RGB phase and not further. Considering this, we compared the ages obtained in the previous Section with ages from `MIST` isochrones and the results were consistent within the errors. Also, as it was proved in Li et al. (2020), age estimates of SG have less model dependence and hence are more reliable than those of MS stars or red giants.

[6]`http://waps.cfa.harvard.edu/MIST/index.html`
[7]`http://mesa.sourceforge.net/`

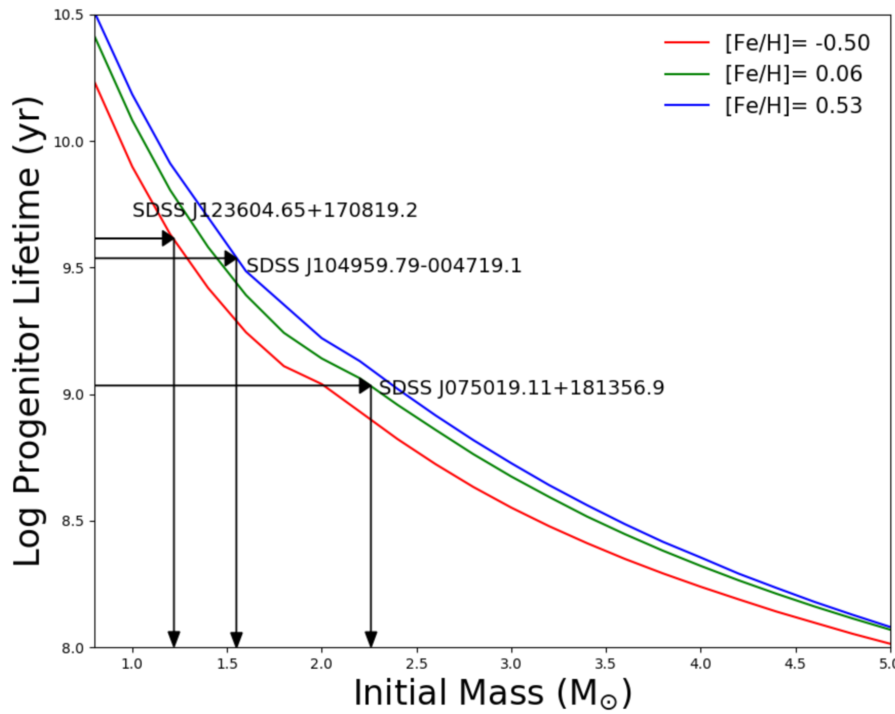

Figure 3.8: Progenitor lifetime function for different metallicities using `MIST` models. Red curve: [Fe/H]= -0.53; green curve: [Fe/H]= 0.06; blue curve: [Fe/H]= +0.5. The black line shows the progenitor lifetime (y axis) mapped into an initial mass (x axis).

To create the PLF, we ran the evolutionary model for initial masses from 0.8 to 8.0 $M_\odot$ in steps of 0.2 $M_\odot$, for different metallicities from +0.50 to -0.53 dex, and with no rotation. We stopped our model at the first thermal pulse (1TP) of the TP-AGB, setting the stars age here as its progenitor lifetime, as evolution through this phase is quick and complex (10^5-10^6 year, or $< 1\%$ of its lifetime), with higher mass stars evolving faster (Vassiliadis and Wood, 1993).

Subsequently, we mapped the progenitor lifetime with the metallicity of each pair into a progenitor mass. The system's metallicity comes from the TO/SG primary because we cannot directly measure this parameter from a WD. Regardless of this, assuming that both stars were born together, means that the chemical composition is similar for them (Andrews et al., 2018, 2019). We can see an example in Fig. 3.8, where the PLFs are the red, green, and blue curves (for [Fe/H]= -0.53, 0.06 and +0.50 respectively); the black arrows indicate the progenitor masses obtained for a given lifetime. The function will change depending on the metallicity, for higher (lower) values, the curve will move to the right (left). Also, we can see that the slope of the curve decreases, while the initial mass increases.

Table 3.7: White Dwarfs Total Ages, Initial and Final Masses for Our Sample.

Object ID (SDSS)	Total Age (Gyr)	τ_{cool} (Gyr)	τ_{prog} (Gyr)	$[Fe/H]_{prog}$	M_f ($M_\odot$)	M_i ($M_\odot$)	WD Ref.
J012824.93-082254.1	$5.61^{+0.60}_{-0.64}$	$1.97^{+0.04}_{-0.04}$	$3.64^{+0.64}_{-0.60}$	-0.14 ± 0.02	0.456 ± 0.070	$1.36^{+0.08}_{-0.06}$	1
		$1.36^{+0.15}_{-0.13}$	$4.25^{+0.62}_{-0.65}$		0.494 ± 0.040	$1.30^{+0.07}_{-0.05}$	2
J123604.65+170819.2	$5.41^{+0.18}_{-0.15}$	$1.30^{+0.52}_{-0.40}$	$4.11^{+0.55}_{-0.43}$	-0.53 ± 0.02	0.819 ± 0.110	$1.21^{+0.05}_{-0.04}$	1
		$1.28^{+0.40}_{-0.25}$	$4.13^{+0.44}_{-0.29}$		0.827 ± 0.065	$1.22^{+0.02}_{-0.04}$	2
J154634.50+233438.0	$2.21^{+0.23}_{-0.76}$	$0.48^{+0.03}_{-0.03}$	$1.73^{+0.23}_{-0.76}$	0.23 ± 0.03	0.696 ± 0.029	$1.89^{+0.53}_{-0.09}$	1
		$0.13^{+0.01}_{-0.01}$	$2.08^{+0.23}_{-0.76}$		0.605 ± 0.011	$1.76^{+0.39}_{-0.06}$	2
J225247.41+270433.7	$2.00^{+0.07}_{-0.12}$	$0.09^{+0.01}_{-0.01}$	$1.91^{+0.07}_{-0.12}$	-0.22 ± 0.02	0.572 ± 0.023	$1.64^{+0.04}_{-0.02}$	1
		$0.10^{+0.01}_{-0.01}$	$1.90^{+0.07}_{-0.12}$		0.580 ± 0.011	$1.65^{+0.04}_{-0.03}$	2
J220850.53+001349.0	$1.40^{+0.46}_{-0.20}$	$0.07^{+0.04}_{-0.02}$	$1.33^{+0.46}_{-0.20}$	-0.22 ± 0.04	0.486 ± 0.239	$1.93^{+0.16}_{-0.25}$	1
		$0.11^{+0.07}_{-0.05}$	$1.29^{+0.47}_{-0.21}$		0.660 ± 0.116	$1.97^{+0.15}_{-0.27}$	2
J001624.09+082157.0	$1.80^{+0.15}_{-0.08}$	$0.13^{+0.01}_{-0.01}$	$1.67^{+0.15}_{-0.08}$	-0.08 ± 0.05	0.544 ± 0.040	$1.77^{+0.04}_{-0.04}$	1
		$0.13^{+0.01}_{-0.01}$	$1.67^{+0.15}_{-0.08}$		0.582 ± 0.001	$1.77^{+0.04}_{-0.04}$	2
J021134.67-000025.9	$11.20^{+0.31}_{-0.89}$	$0.71^{+0.16}_{-0.28}$	$10.49^{+0.35}_{-0.93}$	-0.22 ± 0.02	0.696 ± 0.129	$0.98^{+0.02}_{-0.01}$	1
		$0.91^{+0.04}_{-0.04}$	$10.29^{+0.31}_{-0.89}$		0.842 ± 0.006	$0.98^{+0.02}_{-0.01}$	2
J211928.44-002632.9	$3.58^{+0.04}_{-0.68}$	$0.12^{+0.02}_{-0.06}$	$3.46^{+0.04}_{-0.68}$	-0.27 ± 0.03	0.618 ± 0.148	$1.38^{+0.04}_{-0.04}$	1
		$0.12^{+0.04}_{-0.03}$	$3.46^{+0.06}_{-0.68}$		0.566 ± 0.057	$1.38^{+0.03}_{-0.04}$	2
J075019.11+181356.9	$2.40^{+0.24}_{-0.09}$	$1.01^{+0.11}_{-0.09}$	$1.39^{+0.26}_{-0.13}$	0.06 ± 0.04	0.698 ± 0.042	$2.00^{+0.10}_{-0.15}$	1
		$1.32^{+0.16}_{-0.13}$	$1.08^{+0.29}_{-0.16}$		0.820 ± 0.028	$2.26^{+0.13}_{-0.25}$	2
J104959.79-004719.1	$3.60^{+0.16}_{-0.10}$	$0.17^{+0.01}_{-0.01}$	$3.43^{+0.16}_{-0.10}$	0.49 ± 0.02	0.569 ± 0.026	$1.56^{+0.01}_{-0.02}$	1
		$0.16^{+0.01}_{-0.01}$	$3.44^{+0.16}_{-0.10}$		0.580 ± 0.011	$1.55^{+0.02}_{-0.01}$	2
J115357.30+190606.9	$6.80^{+0.79}_{-0.58}$	$0.58^{+0.15}_{-0.12}$	$6.22^{+0.80}_{-0.59}$	-0.04 ± 0.02	0.740 ± 0.089	$1.18^{+0.04}_{-0.03}$	1
		$0.39^{+0.34}_{-0.17}$	$6.41^{+0.86}_{-0.60}$		0.617 ± 0.127	$1.17^{+0.04}_{-0.03}$	2

Notes. Ref. 1 are WD masses and cooling times reported by Anguiano et al. (2017), and Ref. 2 are WD masses and cooling times obtained in this work using evolutionary models by Fontaine et al. (2001). Initial masses (M_i) are those obtained in this work.

In Table 3.7, we show the spectroscopic final masses (M_f) and initial masses (M_i) estimated in this work. The ages of the systems, WD's cooling times, progenitor lifetimes, and metallicities are also given. As can be seen, all the total ages exceed the cooling times obtained in BA17 (Ref. 1) and this work (Ref. 2). The progenitor lifetimes calculated for both references yielded M_i between 0.98 and 2.26 $M_\odot$. In Fig 3.9, we can see both M_i determination with the two different cooling times following the 1:1 relation, showing consistency within the errors. SDSS J154634.50+233438.0 and SDSS J075019.11+181356.9 are the only WDs with differences over 0.1 $M_\odot$, which is equivalent to a relative difference in M_i of 7.1% and 12.2%, respectively. For most of our sample, the M_i determination has errors better than 6%, except for SDSS J154634.50+233438.0, SDSS J220850.53+001349.0 and SDSS J075019.11+181356.9 with errors between 7.5% and 28%. It is important to notice that the blue dots are M_i calculated using the age of stars outside of the ideal evolutionary phase (see Section 3.2.2).

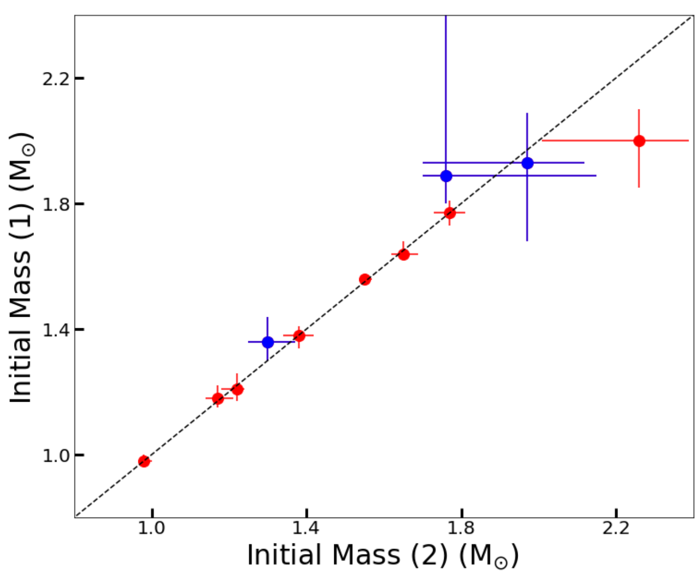

Figure 3.9: Initial mass comparison for our sample. Ref. 1 corresponds to initial masses obtained subtracting cooling times of BA17 (Anguiano et al., 2017) to the system's age, and Ref. 2 subtracted cooling times obtained in this work to the system's age. The blue dots indicate initial masses calculated using the age of stars outside of the ideal evolutionary phase.

Chapter 4

Discussion

4.1 Constraining the Low-Mass End of the Relation

In our sample of WBs, the range in age goes from 1.40 to 11.20 Gyr, in M_i from 0.98 to 2.26 $M_\odot$, and in metallicity from -0.53 to +0.49 dex. Fig. 4.1 displays the resulting semi-empirical constraints for the IFMR using 11 WDs in our sample (red and blue dots), the difference in color comes from the age determination, in particular, the blue dots are constraints calculated using the age of stars outside of the ideal evolutionary phase. For the sake of comparison, the figure has 2 panels, the first one using the WD's masses and cooling times by BA17 (top panel), and the other using WD's masses and cooling times calculated in this work (bottom panel). Both plots include constraints found by Catalán et al. (2008b) and Zhao et al. (2012) using MS-WD binaries (grey squares). Also, we show a theoretical IFMR by Weiss and Ferguson (2009) (dashed line), IFMR by Andrews et al. (2015) using wide WD-WD binaries (dotted line) and empirical IFMR by El-Badry et al. (2018) using field WDs (solid line).

From an inspection of Fig. 4.1, we notice that all the points found in this work using TO/SG-WD binaries have $M_i < 2.5$ $M_\odot$, allowing us to better constrain the IFMR in the low-mass end, which is a difficult limit to reach using OCs, and a similar region that was weakly constraint previously using MS-WD binaries by Catalán et al. (2008b) and Zhao et al. (2012). If we look at the M_i uncertainties, the constraints found by MS-WD binaries have large error bars. This is because of the poor accuracy

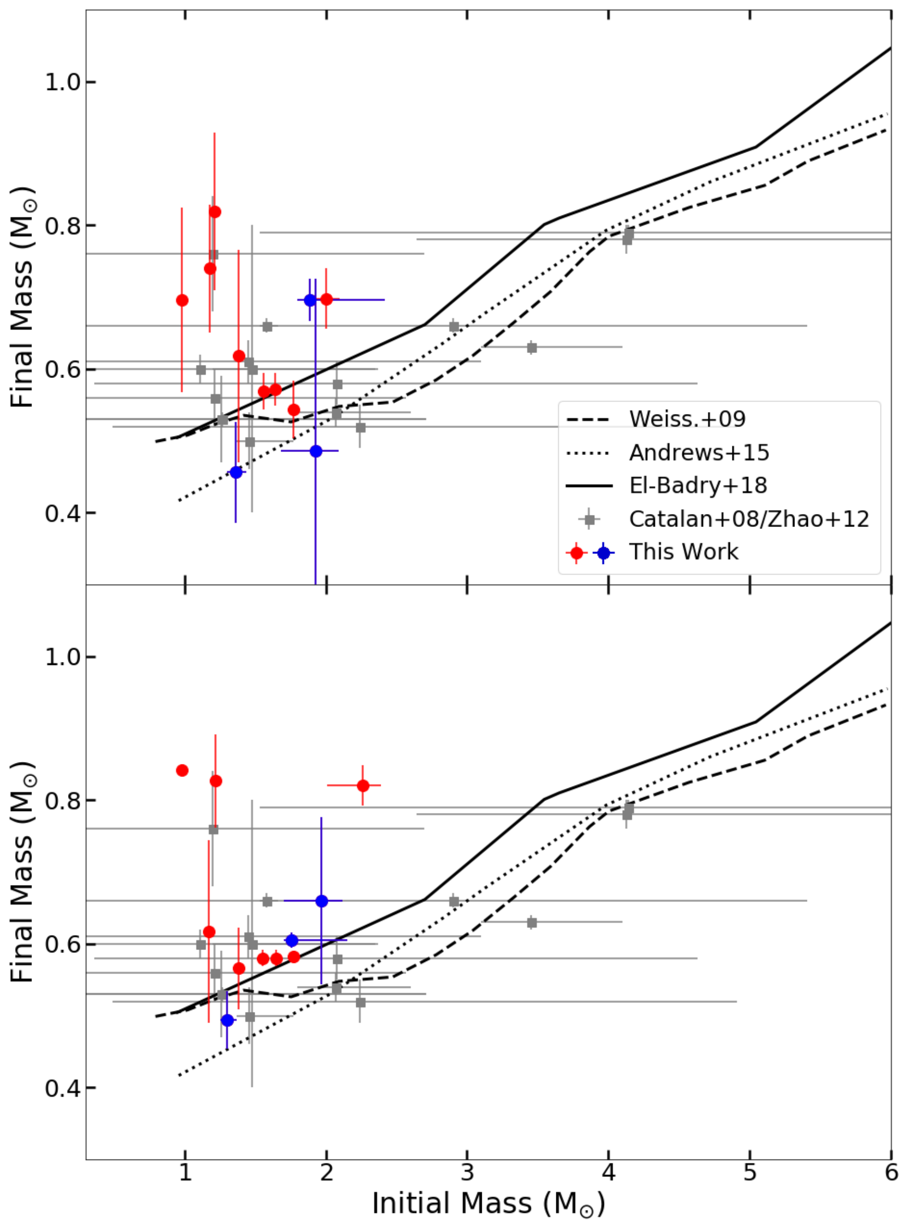

Figure 4.1: Constraints for the IFMR obtained in this work. Top panel: Constraints found using WD's masses and cooling times from BA2017. Bottom panel: Constraints found using WD's masses and cooling times obtained in this work. Grey squares are constraints from Catalán et al. (2008b) and Zhao et al. (2012), red and blue dots are constraints found in this work. The dashed line is the theoretical IFMR by Weiss and Ferguson (2009), the solid line is the IFMR by El-Badry et al. (2018) and Andrews et al. (2015) relation is the dotted line.

obtaining ages for MS stars using isochrones, as we discussed in Section 3.2.2. In Catalán et al. (2008b), the errors for this parameter are between 18% and 59% in most of the sample. In Zhao et al. (2012), almost all the uncertainties are between 12% and 25% and one case with an error of 93%. In contrast, the errors reported in this work are mostly under 6%, and three M_i have uncertainties between 7.5% and 28%, improving considerably the previous results using the WB method.

Also, we have the IFMRs presented by Weiss and Ferguson (2009), Andrews et al. (2015) and El-Badry et al. (2018). The theoretical relation of Weiss and Ferguson (2009) traces a linear fit between the initial and final mass, being flatter between $1.2 < M_i/M_\odot < 2.5$, yielding WD's masses around 0.55 $M_\odot$. The slope of the line becomes steeper for M_i between 2.5 and 4 $M_\odot$ and then gets smoother above 4 $M_\odot$. A similar trace can be seen in the case of El-Badry et al. (2018), but yielding bigger WD's masses than Weiss and Ferguson (2009) for $M_i > 1.2$ $M_\odot$. For this IFMR, the slope increases rapidly between $2.8 < M_i/M_\odot < 3.7$, obtaining WDs' masses between 0.6 and 0.8 $M_\odot$. Andrews et al. (2015) relation yields smaller masses than the other two IFMRs under 2 $M_\odot$. The change in the slope is not as strong here as in the other cases. Looking at both panels of Fig. 4.1, we can say that El-Badry et al. (2018) fits our points in the M_i range from 1.2 to 2.0 $M_\odot$. However, the more massive WDs in our sample show a different behavior. The relations from Weiss and Ferguson (2009) and Andrews et al. (2015) go under our constraints.

Taking a look at the bottom panel of Fig. 4.1 a progenitor star of $M_i \approx 1.20$ $M_\odot$ (cf. SDSS J115357.30 and SDSS J123604.65), could end up as WDs with masses that differ by ≈ 0.21 $M_\odot$; while in the top panel, for the same progenitor mass and WDs the difference is around 0.12 $M_\odot$. Moreover, in the bottom panel two WDs of nearly the same mass (≈ 0.83 $M_\odot$) could come from progenitor stars with masses different by a factor of 2 (cf. SDSS J021134.67 and SDSS J075019.11); while in the top panel for the same WDs, in this case with $M_f \approx 0.70$ $M_\odot$, the difference in initial mass remains the same (≈ 1 $M_\odot$). Taking this into account, the robustness of the constraints in our work will depend on the M_f determination, hence, on the WD's spectra quality (or WD's photometry). For low S/N spectra, atmospheric parameters are less accurate, and therefore, WD's cooling times and masses will have bigger uncertainties. This is one of the weakest points of studying WDs spectroscopically. With the use of SG-WD binaries, we are not limited anymore by the precision in M_i, but now the pressure is on M_f, i.e., the mass of the WD today.

Overall, our constraints show a dispersion in the final mass for initial masses below 2.5 $M_\odot$. Also, both panels show a group of WDs with larger M_f than expected based in theory. For these systems with massive WDs, it would be ideal to confirm their binarity. This can be done by having more than one spectroscopic epoch for both components and performing spectral analysis to check variations in radial velocities (for the SG) and in the H_α spectral feature (for the WD). Also, we could obtain better spectroscopic parameters to check the masses or use other methods such as the gravitational redshift to yield masses using the radial velocities of both binary components as it was done by Silvestri et al. (2001). This will be left as future work.

4.2 Complementing with Open and Globular Clusters

We plotted our points (red and blue dots) along with the constraints presented in Cummings et al. (2018) for OCs and Globular Clusters (GCs; grey dots and solid line fitted) as we can see in Fig. 4.2. WD progenitors from OCs have metallicities between -0.14 to +0.15 dex and the constraints populate mostly the upper mass limit, with M_i between 2.75 and 6.0 $M_\odot$, yielding WDs' masses from 0.70 to 1.10 $M_\odot$. On the lower part of the figure, all the points around $M_i \approx 0.80$ $M_\odot$ and $M_f \approx 0.55$ $M_\odot$ correspond to WDs in GCs, the metallicity for this WDs progenitors is -1.10 dex and they are the oldest stars in the whole sample. Using WDs in GCs to constrain the IFMR is a challenging task. These stellar groups are old, and the cooling sequences of WDs are typically fainter than magnitude 22 in the V band, making spectroscopic observations extremely hard. Thus, just a handful of WDs in GCs can be used to study this relationship. Overall, stellar cluster constraints cover a different mass region than the constraints found in this work using TO/SG-WD binaries.

OC and GC constraints reported by Cummings et al. (2018) produce more massive WDs for an arbitrary M_i in comparison with the other IFMRs. However, the points and the fitted line show a similar shape with the IFMR by El-Badry and Rix (2018), especially in the mass range from 2.5 to 4.0 $M_\odot$. This "knee" in the IFMR seem to be present in the other references too, but for lower WD's masses. In fact, this shape is predicted by stellar evolution models due to the onset of the helium flash at $M_i \lesssim 2$ $M_\odot$ and the effects of second dredge-up at $M_i \gtrsim 4$ $M_\odot$ (e.g. Choi et al., 2016). From 4 $M_\odot$ to the high-mass end, the constraints show a larger dispersion but still, an actual relationship is apparent, and the data is well fitted.

Looking at the low-mass end in Fig 4.2, we can see a linear fit with a constant slope from 0.83 to 3.00 $M_\odot$. The lower limit of the relation is well constrained given the GC's points at $M_i \approx 0.83$ $M_\odot$. On the other hand, between 1 and 2 $M_\odot$ the fit is done with just 5 points with a scatter of $\Delta M_f \approx 0.15$ $M_\odot$ for $M_i \approx 1.80$ $M_\odot$. This speaks about the limitation on constraining this range of masses using stellar clusters, and the need for WBs to populate the IFMR at the low-mass end. Our constraints between $1 < M_i < 2$ $M_\odot$ fill this void in the semi-empirical IFMR.

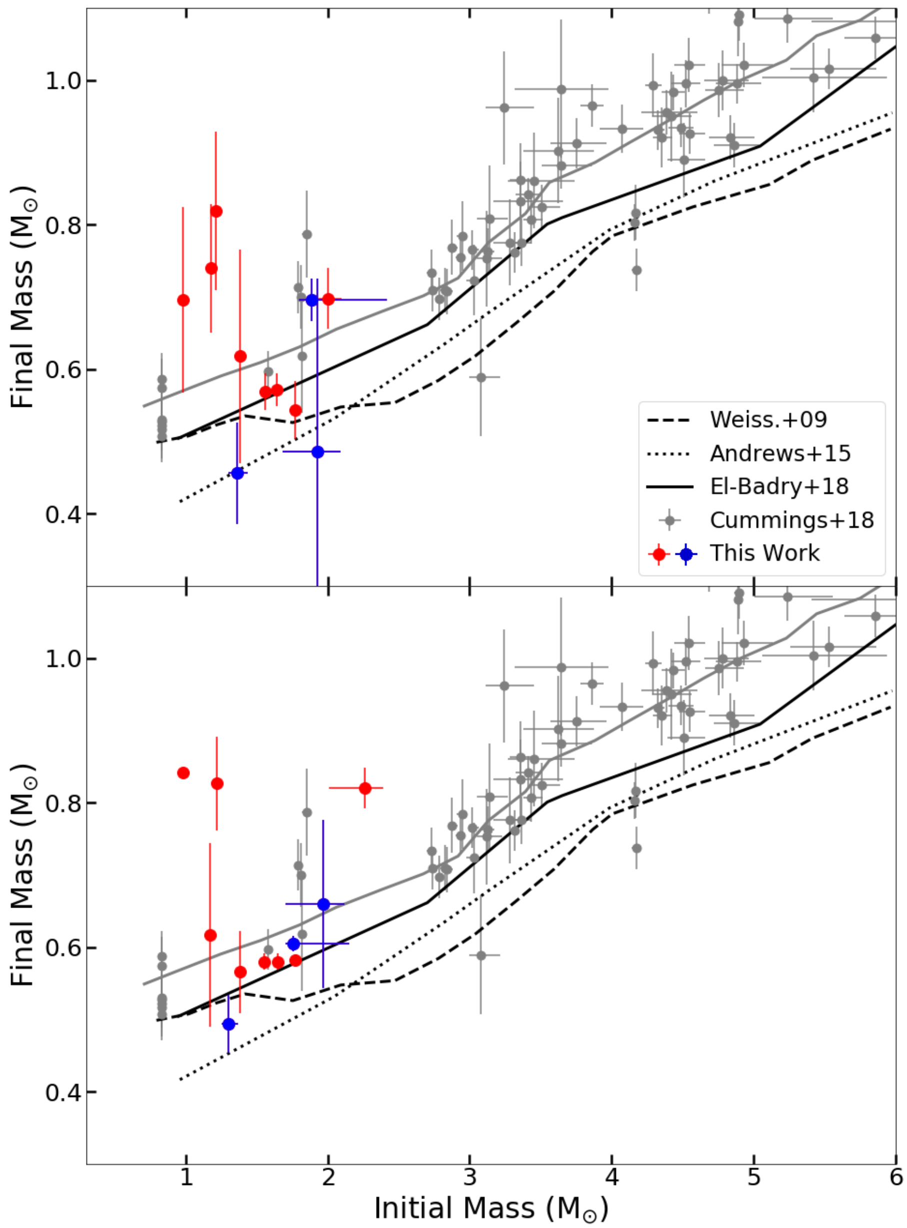

Figure 4.2: IFMR from OC's WDs and constraints from this work. Top panel: Constraints found using WD's masses and cooling times from BA2017. Bottom panel: Constraints found using WD's masses and cooling times obtained in this work. Grey dots and solid line show the constraints by Cummings et al. (2018), red and blue dots are constraints for this work. The black solid line is the IFMR by El-Badry et al. (2018), dotted line is the IFMR by Andrews et al. (2015) and dashed lines is a theoretical IFMR Weiss and Ferguson (2009).

4.3 Metallicity Dependency

Previous studies of the IFMR have tried to understand the scatter found in this relation. One of the clues that seem to be relevant is the metallicity. There are theoretical and observational studies trying to understand how this parameter affects the mass-loss in stars, especially at late evolutionary stages. For example, a theoretical study by Renedo et al. (2010) found that metal-poor stars undergo more thermal pulses on the AGB, increasing the core mass, resulting in more massive WDs. Weiss and Ferguson (2009) predicted IFMRs for different metallicities from -1.6 $<$ [Fe/H] $<$ +0.3, the results showed that for M_i below 2 $M_\odot$, the WDs' masses were $\approx$ 0.52 $M_\odot$; for M_i over 2 $M_\odot$, metal poor relations yielded bigger M_f. We can associate this prediction with a bigger mass loss for metal rich stars. Also, Choi et al. (2016) predicted a similar behavior, but the WDs' masses below 2 $M_\odot$ increased slowly from 0.5 to 0.6 $M_\odot$.

In addition, observational studies as the one from Kalirai et al. (2005) suggested that the low metallicity ([Fe/H] = 0) of M37 might result in less mass loss on the AGB and, therefore, more massive WDs. Kalirai et al. (2007) found evidence for enhanced mass loss at extremely high metallicities by studying the WD mass distribution in the super-solar metallicity star cluster NGC 6791 ([Fe/H] = +0.40). Zhao et al. (2012) using a sample of 12 WBs to study the IFMR with metallicities -0.40 $<$ [Fe/H] $<$ +0.19, suggested that this parameter plays an important role in the amount of mass lost during post-MS evolution. On the other hand, Catalán et al. (2008a) concluded that the scatter in the IFMR is not an effect of metallicity. Cummings et al. (2018) found that there is no detectable metallicity dependence across the range of -0.15 $<$ [Fe/H] $<$ +0.15 for stars from 2.75 to 6 $M_\odot$ in OCs. Other works as Andrews et al. (2015) using wide WD-WD binaries, and El-Badry et al. (2018) which uses field WDs, cannot conclude anything about metallicity effects because is impossible to measure this value directly from the WDs, they assumed solar metallicities.

For our sample of TO/SG-WD binaries, the metallicities are between -0.50 and +0.50 dex, a slightly bigger range than Zhao et al. (2012) and OCs constraints at Cummings et al. (2018). In Fig. 4.3 we can see the dependence of the mass loss with the M_i of the WD progenitors. While M_i increases from 1 to 1.5 $M_\odot$, for our WD

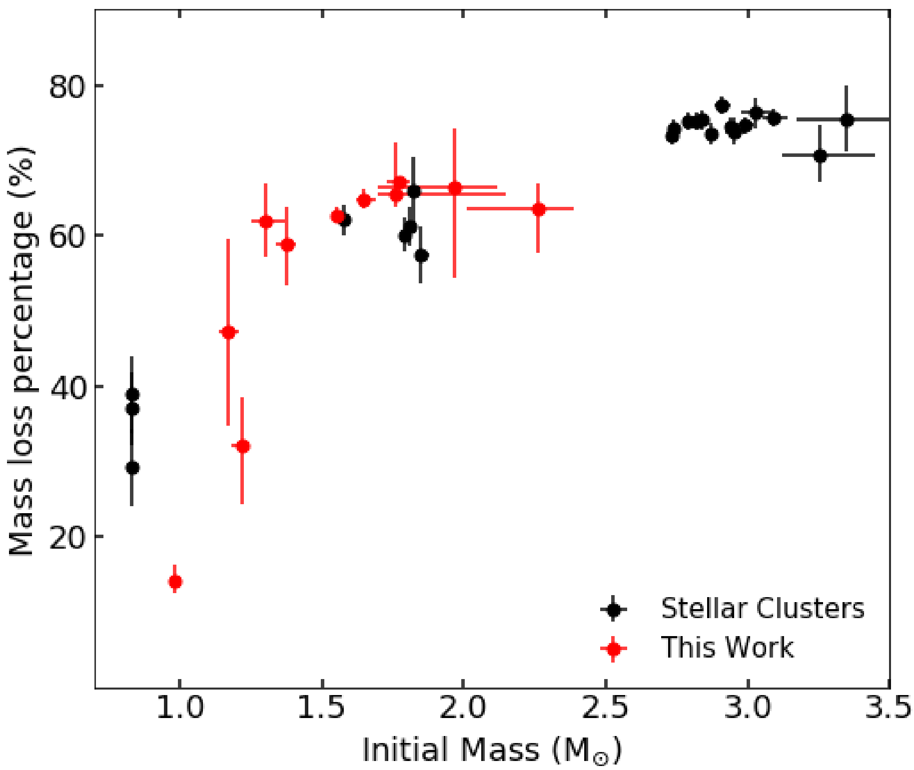

Figure 4.3: Mass loss percentage vs Initial Mass for each WD progenitor in our sample. Red dots are WDs in our sample and Black dots are WDs in stellar clusters (OCs and GCs).

progenitors (red dots) the mass loss grows from 14% to $\approx$ 65%, after this, from 1.5 to 2.5 $M_\odot$ the mass loss seem to be almost constant. Also, one of our WD progenitors shows a deficit of mass loss compared with the stellar cluster data (black dots). In terms of the relationship between mass loss and metallicity, we cannot obtain any correlation with the data we have. We would need to analyze a bigger sample of WD progenitors with similar masses and different metallicities to conclude about this topic, and it will be left as future work.

Chapter 5

Summary and Future Work

In this work, we have studied a sample of 11 WBs comprised of a TO/SG primary and a secondary white dwarf. This sample was selected by matching the SDSS DR12 WD catalog with the *Gaia* astrometric surveys. For the primaries, we have performed independent high-resolution spectroscopic observations. The excitation/ionization balance technique helped us to determine $T_{\rm eff}$, log g, and [Fe/H] using the spectral synthesis code MOOG. Then, with these atmospheric parameters, we calculated system ages via theoretical isochrones of $\mathtt{Y}^2$. For the secondaries, we took $T_{\rm eff}$ and log g from the literature in BA17 (Anguiano et al., 2017), KL13 (Kleinman et al., 2013) and KE1516 (Kepler et al., 2015, 2016). The former reported masses and cooling times using Althaus et al. (2010) and Renedo et al. (2010) cooling tracks. To compare these parameters, we obtained masses and cooling times using cooling sequences from F01 (Fontaine et al., 2001) in the MWDD. Finally, having system ages and cooling times for the WDs, we were able to calculate their progenitor lifetimes. Then, using metallicities and stellar evolution models, we found initial masses for 11 WD's progenitors, all below 2.5 $M_\odot$.

With the estimated initial mass and the spectroscopic final mass, we constrained the low-mass end of the IFMR, a range that has been poorly covered by stellar cluster data, and poorly constrained by previous studies using WBs. Our constraints show a significant improvement in the initial mass determination compared with those from Catalán et al. (2008b) and Zhao et al. (2012), with errors better than 6% in almost all our WD's progenitors because of the accuracy in our measured ages (better than 12% in almost all the sample). On the other hand, the spectroscopic determination of masses and cooling times have bigger uncertainties for those WDs with low S/N spectra. Thus, the robustness of our constraints depends directly on the final mass determination. With the use of SG-WD binaries, we are not limited anymore by the precision in initial mass, but now the pressure is on the mass of the WD today. In addition, we can say that there is a dispersion in final mass for initial masses between 1.0 and 2.5 $M_\odot$. This scatter in the observational data seem to be a real effect, rather than a consequence of the uncertainties in the final mass estimates. In terms of metallicity, we did not find any trend or correlation between mass loss and this parameter for our sample.

5.1 Future work

As future work, it would be interesting to confirm the binarity of the pairs with more massive WDs in our sample. For these systems with massive WDs, it would be ideal to confirm their binarity. This can be done by having more than one spectroscopic epoch for both components and performing spectral analysis to check variations in radial velocities (for the SG) and in the H_α spectral feature (for the WD). Also, we could obtain better spectroscopic parameters to check the masses or use other methods such as the gravitational redshift to yield masses using the radial velocities of both binary components as it was done by Silvestri et al. (2001). In terms of the relationship between mass loss and metallicity, we would need to analyze a bigger sample of WD progenitors with similar masses and different metallicities to conclude about this topic.

To expand our sample of TO/SG binaries, we are already working in a telescope proposal for 2020B semester using the new WB catalog from El-Badry and Rix (2018) to constraint the IFMR. This catalog reported three different types of WBs including pairs of MS-WD and WD-WD. The MS-WD binaries in the catalog also contain TO and SG stars as primaries. An example of our target selection for this proposal can be seen in Fig. 5.1, where the red dots are SG-WD pairs and blue dots are WD-WD pairs, the grey background is the full sample of MS-WD binaries by El-Badry and Rix (2018), and the green lines show the SG's selection zone. With these new data we are planning on constraint the IFMR with both types of binaries mentioned before. Hopefully we can get the necessary time to observe these targets.

Additionally, we are looking forward to cross-match new WD catalogs such as Gentile Fusillo et al. (2019) with stars in *Gaia* following the steps showed in Chapter 2. With a bigger sample of WBs, it would be possible to fill the lower and intermediate-mass end of the IFMR with strong constraints as we demonstrated in this thesis. Furthermore, we aim to study metallicity and rotation effects in the IFMR. On the other hand, it would be interesting to verify if there is any difference in our results using photometric parameters instead of spectroscopic parameters for the WDs. Recently, studies have shown that photometric method can achieve a similar accuracy as the spectroscopic method (see Gentile Fusillo et al., 2019; Kilic et al., 2019). In this way, we can increase our universe of WDs and add a new way of studying the IFMR, taking advantage of precise parallaxes from *Gaia* and magnitudes from different surveys.

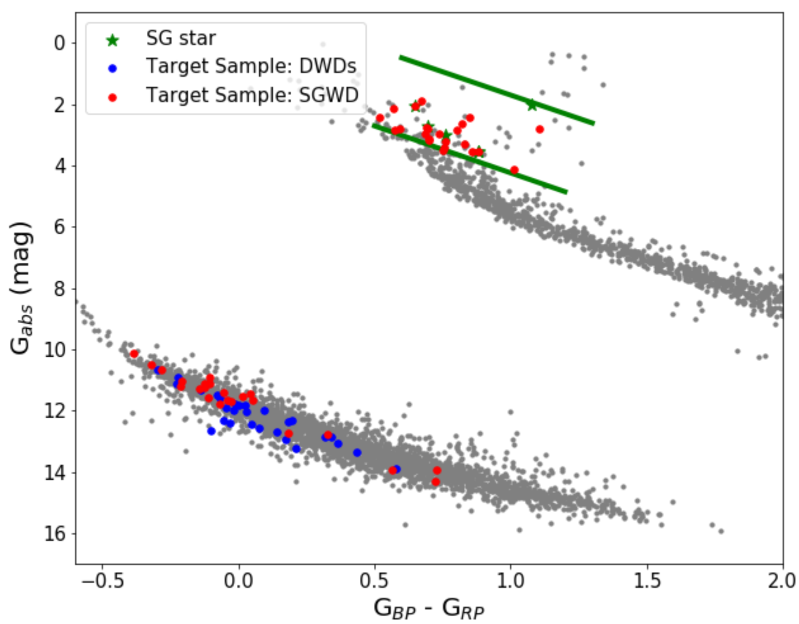

Figure 5.1: Color-Magnitude Diagram using *Gaia* magnitudes, showing our sample selection for 2020B semester. Red dots are SG-WD binaries, blue dots are WD-WD binaries, grey background is the MS-WD catalog by El-Badry and Rix (2018). The green lines indicate the selection zone of SGs.

Appendix A

Comparison with Literature Atmospheric Parameters

For our sample of TO/SG in TGAS, we could not find many references with spectroscopic atmospheric parameters. We searched in catalogs such as PASTEL (Soubiran et al., 2016), which is a bibliographical compilation of stellar atmospheric parameters (T_{eff}, log g, [Fe/H]) relying on high-resolution, high signal-to-noise spectroscopy, but non of the stars in our sample was there. We found four stars in The Large Sky Area Multi-Object Fiber Spectroscopic Telescope DR4 (LAMOST; Luo et al., 2015), with effective temperatures, surface gravities, and metallicities. We can see these parameters in Table A.1. This project determines the atmospheric parameters using low resolution spectra (R=1800). This literature sample is too small to do a comparison, therefore, we also included photometric effective temperatures presented in *Gaia* DR2. If we look at effective temperatures in Fig. A.1, all of them show consistency within the error bars. Metallicities and surface gravities show consistency with our results, except for star TYC 823-447-1 is the only star with larger differences. This is expected because of the bad quality of the atmospheric parameters in this case.

Table A.1: Comparing Atmospheric Parameters for the Observed Primary Stars in our Wide Binaries

Object ID (TYC)	T_{eff} (K)	log g (cm s^{-2})	[Fe/H] (dex)	Ref.
5274-489-1	6009 ± 32	4.20 ± 0.06	-0.14 ± 0.02	1
	6043 ± 21	4.27 ± 0.03	-0.17 ± 0.02	2
	5996 ± 216	-	-	3
1446-1524-1	5958 ± 28	3.95 ± 0.08	-0.53 ± 0.02	1
	5817 ± 162	-	-	3
2033-5-1	6179 ± 32	4.22 ± 0.07	0.23 ± 0.03	1
	5977 ± 410	-	-	3
2229-1088-1	5151 ± 24	3.34 ± 0.08	-0.22 ± 0.02	1
	5066 ± 68	-	-	3
558-2215-1	4849 ± 48	2.50 ± 0.16	-0.22 ± 0.04	1
	4827 ± 123	-	-	3
595-764-1	6564 ± 83	3.90 ± 0.15	-0.08 ± 0.05	1
	6376 ± 171	-	-	3
38-358-1	5723 ± 29	4.11 ± 0.06	-0.22 ± 0.02	1
	5669 ± 25	4.14 ± 0.04	-0.26 ± 0.02	2
	5738 ± 248	-	-	3
5194-1015-1	6353 ± 46	3.99 ± 0.09	-0.27 ± 0.03	1
	6246 ± 505	-	-	3
823-447-1	6668 ± 131	4.53 ± 0.22	0.11 ± 0.08	1
	6562 ± 17	4.23 ± 0.02	-0.09 ± 0.01	2
	6784 ± 265	-	-	3
1366-1363-1	6408 ± 64	4.01 ± 0.10	0.06 ± 0.04	1
	6376 ± 206	-	-	3
4723-595-1	5880 ± 19	4.45 ± 0.06	-0.31 ± 0.02	1
	5843 ± 44	-	-	3
4913-1024-1	5798 ± 23	4.19 ± 0.04	0.49 ± 0.02	1
	5708 ± 27	3.93 ± 0.04	0.46 ± 0.02	2
	5591 ± 100	-	-	3
1443-1882-1	5281 ± 19	3.88 ± 0.05	-0.04 ± 0.02	1

References. 1: This work; 2: Luo et al. (2015) ; 3: Gaia Collaboration et al. (2018).

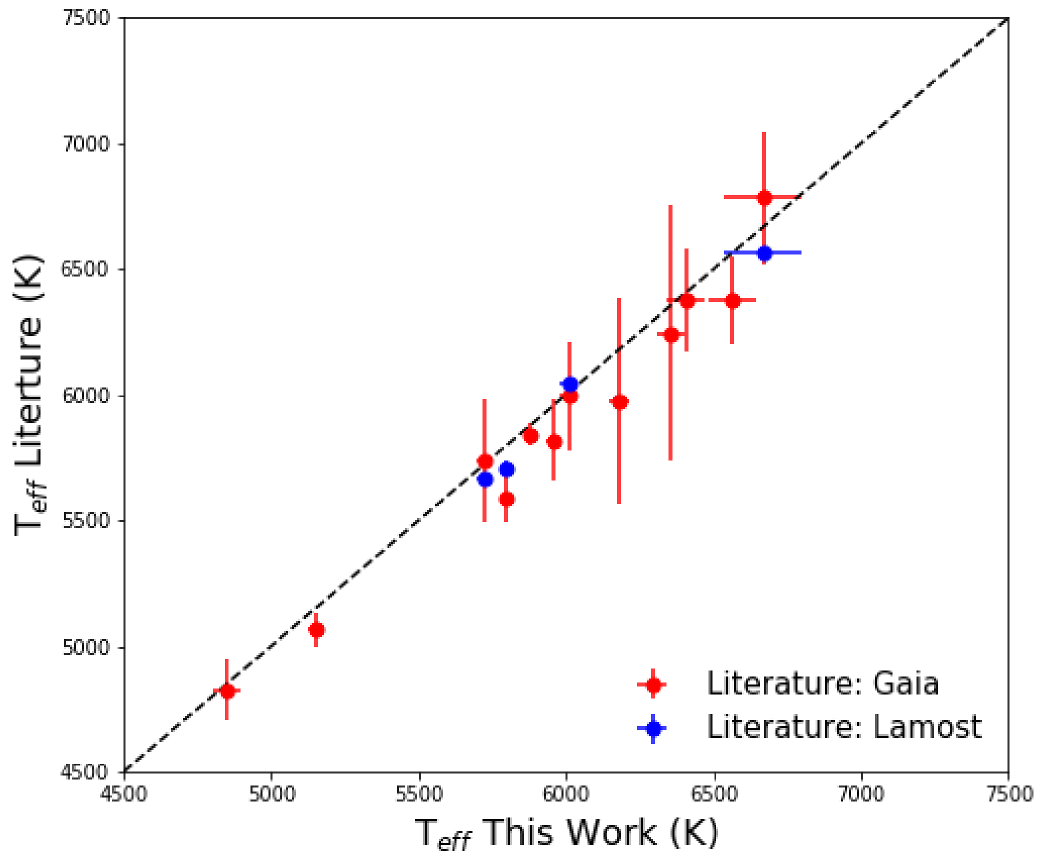

Figure A.1: Effective temperatures comparison for our primaries. Red dots are our spectroscopic temperatures vs photometric temperatures from *Gaia*, and blue dots are our spectroscopic temperatures vs spectroscopic temperatures from LAMOST.

Appendix B

Binning Test for Age Determination

Here we explain briefly how we selected the binning in the age determination. If we look at Fig B.1, for 0.2 Gyr bin and 0.5 Gyr bin the ages determined are similar with differences around 0.1-0.2 Gyr, but the latter can overestimate the errors in not-completely Gaussian distributions. On the other hand, for bins over 0.5 Gyr, the sensitivity in the age determination is loss, and because of the evolutionary state of our stars the precision should be better than 1 Gyr, probably yielding a wrong age. Therefore, we chose the 0.2 Gyr bin that allows us to achieve ages and uncertainties consistent with the Bayesian method as we showed in Section 3.2.2.

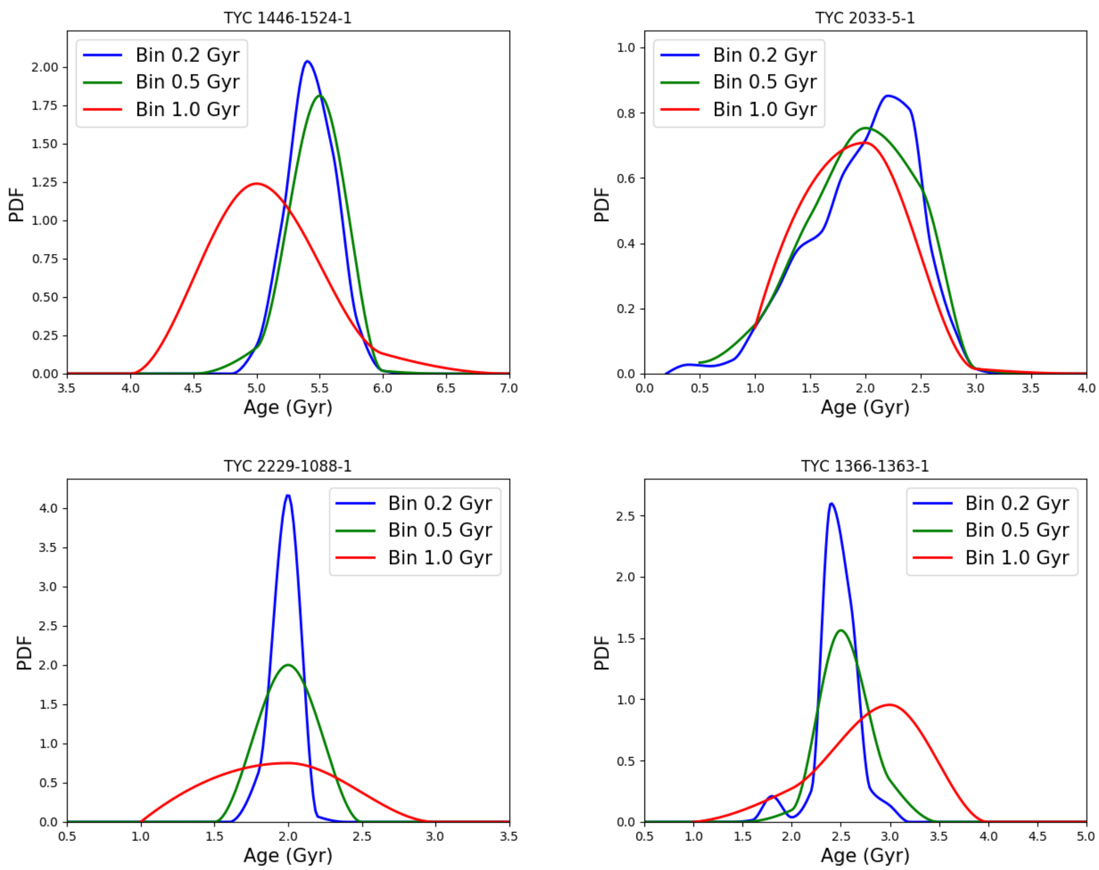

Figure B.1: Binning test for age determination. Here we show the age of 4 stars in our sample using 3 different binnings. Blue curve corresponds to a 0.2 Gyr bin, green curve corresponds to a 0.5 Gyr bin and red curve corresponds to a 1.0 Gyr bin.

Bibliography

Allende Prieto, C., Barklem, P. S., Lambert, D. L., and Cunha, K. (2004). S^4N: A spectroscopic survey of stars in the solar neighborhood. The Nearest 15 pc. A&A, 420:183–205.

Althaus, L. G., Córsico, A. H., Isern, J., and García-Berro, E. (2010). Evolutionary and pulsational properties of white dwarf stars. A&A Rev., 18:471–566.

Andrews, J. J., Agüeros, M. A., Gianninas, A., Kilic, M., Dhital, S., and Anderson, S. F. (2015). Constraints on the Initial-Final Mass Relation from Wide Double White Dwarfs. ApJ, 815:63.

Andrews, J. J., Anguiano, B., Chanamé, J., Agüeros, M. A., Lewis, H. M., Hayes, C. R., and Majewski, S. R. (2019). Using APOGEE Wide Binaries to Test Chemical Tagging with Dwarf Stars. ApJ, 871(1):42.

Andrews, J. J., Chanamé, J., and Agüeros, M. A. (2017). Wide binaries in Tycho-Gaia: search method and the distribution of orbital separations. MNRAS, 472:675–699.

Andrews, J. J., Chanamé, J., and Agüeros, M. A. (2018). Wide binaries in Tycho-Gaia II: metallicities, abundances and prospects for chemical tagging. MNRAS, 473(4):5393–5406.

Anguiano, B., Rebassa-Mansergas, A., García-Berro, E., Torres, S., Freeman, K. C., and Zwitter, T. (2017). The kinematics of the white dwarf population from the SDSS DR12. MNRAS, 469:2102–2120.

Asplund, M., Grevesse, N., Sauval, A. J., and Scott, P. (2009). The Chemical Composition of the Sun. ARA&A, 47:481–522.

Barklem, P. S., Stempels, H. C., Allende Prieto, C., Kochukhov, O. P., Piskunov, N., and O'Mara, B. J. (2002). Detailed analysis of Balmer lines in cool dwarf stars. A&A, 385:951–967.

Bergeron, P., Saffer, R. A., and Liebert, J. (1992). A Spectroscopic Determination of the Mass Distribution of DA White Dwarfs. ApJ, 394:228.

Bernstein, R., Shectman, S. A., Gunnels, S. M., Mochnacki, S., and Athey, A. E. (2003). MIKE: A Double Echelle Spectrograph for the Magellan Telescopes at Las Campanas Observatory. In Iye, M. and Moorwood, A. F. M., editors, *Instrument Design and Performance for Optical/Infrared Ground-based Telescopes*, volume 4841 of Proc. SPIE, pages 1694–1704.

Bressan, A., Marigo, P., Girardi, L., Salasnich, B., Dal Cero, C., Rubele, S., and Nanni, A. (2012). PARSEC: stellar tracks and isochrones with the PAdova and TRieste Stellar Evolution Code. MNRAS, 427:127–145.

Catalán, S., Isern, J., García-Berro, E., and Ribas, I. (2008a). The initial-final mass relationship of white dwarfs revisited: effect on the luminosity function and mass distribution. MNRAS.

Catalán, S., Isern, J., García-Berro, E., Ribas, I., Allende Prieto, C., and Bonanos, A. Z. (2008b). The initial-final mass relationship from white dwarfs in common proper motion pairs. A&A.

Chanamé, J. and Ramírez, I. (2012). Toward Precise Ages for Single Stars in the Field. Gyrochronology Constraints at Several Gyr Using Wide Binaries. I. Ages for Initial Sample. ApJ, 746:102.

Choi, J., Dotter, A., Conroy, C., Cantiello, M., Paxton, B., and Johnson, B. D. (2016). Mesa Isochrones and Stellar Tracks (MIST). I. Solar-scaled Models. ApJ, 823:102.

Cummings, J. D., Kalirai, J. S., Tremblay, P.-E., Ramirez-Ruiz, E., and Choi, J. (2018). The White Dwarf Initial-Final Mass Relation for Progenitor Stars from 0.85 to 7.5 M . ApJ, 866:21.

da Silva, L., Girardi, L., Pasquini, L., Setiawan, J., von der Lühe, O., de Medeiros, J. R., Hatzes, A., Döllinger, M. P., and Weiss, A. (2006). Basic physical parameters of a selected sample of evolved stars. A&A, 458:609–623.

Demarque, P., Woo, J.-H., Kim, Y.-C., and Yi, S. K. (2004). Y^2 Isochrones with an Improved Core Overshoot Treatment. ApJS, 155:667–674.

Dobbie, P. D., Napiwotzki, R., Burleigh, M. R., Barstow, M. A., Boyce, D. D., Casewell, S. L., Jameson, R. F., Hubeny, I., and Fontaine, G. (2006). New Praesepe white dwarfs and the initial mass-final mass relation. MNRAS, 369:383–389.

Dominguez, I., Chieffi, A., Limongi, M., and Straniero, O. (1999). Intermediate-Mass Stars: Updated Models. ApJ, 524(1):226–241.

Dotter, A. (2016). MESA Isochrones and Stellar Tracks (MIST) 0: Methods for the Construction of Stellar Isochrones. ApJS, 222:8.

Dufour, P., Blouin, S., Coutu, S., Fortin-Archambault, M., Thibeault, C., Bergeron, P., and Fontaine, G. (2017). The Montreal White Dwarf Database: A Tool for the Community. In Tremblay, P.-E., Gaensicke, B., and Marsh, T., editors, *20th European White Dwarf Workshop*, volume 509 of *Astronomical Society of the Pacific Conference Series*, page 3.

El-Badry, K. and Rix, H.-W. (2018). Imprints of white dwarf recoil in the separation distribution of Gaia wide binaries. MNRAS, 480(4):4884–4902.

El-Badry, K., Rix, H.-W., and Weisz, D. R. (2018). An Empirical Measurement of the Initial-Final Mass Relation with Gaia White Dwarfs. ApJ, 860(2):L17.

Fontaine, G., Brassard, P., and Bergeron, P. (2001). The Potential of White Dwarf Cosmochronology. PASP, 113:409–435.

Fontaine, G., Villeneuve, B., and Wilson, J. (1981). On the acoustic flux of Sirius A. ApJ, 243:550–556.

Gaia Collaboration, Brown, A. G. A., Vallenari, A., Prusti, T., de Bruijne, J. H. J., Babusiaux, C., Bailer-Jones, C. A. L., Biermann, M., Evans, D. W., Eyer, L., and et al. (2018). Gaia Data Release 2. Summary of the contents and survey properties. A&A, 616:A1.

Gaia Collaboration, Prusti, T., de Bruijne, J. H. J., Brown, A. G. A., Vallenari, A., Babusiaux, C., Bailer-Jones, C. A. L., Bastian, U., Biermann, M., Evans, D. W., and et al. (2016). The Gaia mission. A&A, 595:A1.

Gentile Fusillo, N. P., Tremblay, P.-E., Gänsicke, B. T., Manser, C. J., Cunningham, T., Cukanovaite, E., Hollands, M., Marsh, T., Raddi, R., Jordan, S., Toonen, S., Geier, S., Barstow, M., and Cummings, J. D. (2019). A Gaia Data Release 2 catalogue of white dwarfs and a comparison with SDSS. MNRAS, 482:4570–4591.

Godoy-Rivera, D. and Chanamé, J. (2018). On the identification of wide binaries in the Kepler field. MNRAS, 479:4440–4469.

Greenstein, J. L. (1986). White dwarfs in wide binaries. I - Physical properties. II - Double degenerates and composite spectra. AJ, 92:859–877.

Gustafsson, B., Edvardsson, B., Eriksson, K., Jørgensen, U. G., Nordlund, Å., and Plez, B. (2008). A grid of MARCS model atmospheres for late-type stars. I. Methods and general properties. A&A, 486:951–970.

Jiang, Y.-F. and Tremaine, S. (2010). The evolution of wide binary stars. MNRAS, 401:977–994.

Jørgensen, B. R. and Lindegren, L. (2005). Determination of stellar ages from isochrones: Bayesian estimation versus isochrone fitting. A&A, 436(1):127–143.

Kalirai, J. S., Bergeron, P., Hansen, B. M. S., Kelson, D. D., Reitzel, D. B., Rich, R. M., and Richer, H. B. (2007). Stellar Evolution in NGC 6791: Mass Loss on the Red Giant Branch and the Formation of Low-Mass White Dwarfs. ApJ, 671:748–760.

Kalirai, J. S., Richer, H. B., Reitzel, D., Hansen, B. M. S., Rich, R. M., Fahlman, G. G., Gibson, B. K., and von Hippel, T. (2005). The Initial-Final Mass Relationship: Spectroscopy of White Dwarfs in NGC 2099 (M37). ApJ, 618:L123–L127.

Kepler, S. O., Pelisoli, I., Koester, D., Ourique, G., Kleinman, S. J., Romero, A. D., Nitta, A., Eisenstein, D. J., Costa, J. E. S., Külebi, B., Jordan, S., Dufour, P., Giommi, P., and Rebassa-Mansergas, A. (2015). New white dwarf stars in the Sloan Digital Sky Survey Data Release 10. MNRAS, 446:4078–4087.

Kepler, S. O., Pelisoli, I., Koester, D., Ourique, G., Romero, A. D., Reindl, N., Kleinman, S. J., Eisenstein, D. J., Valois, A. D. M., and Amaral, L. A. (2016). New white dwarf and subdwarf stars in the Sloan Digital Sky Survey Data Release 12. MNRAS, 455:3413–3423.

Kepler, S. O., Pelisoli, I., Koester, D., Reindl, N., Geier, S., Romero, A. D., Ourique, G., Oliveira, C. d. P., and Amaral, L. A. (2019). White dwarf and subdwarf stars in the Sloan Digital Sky Survey Data Release 14. MNRAS, 486:2169–2183.

Kilic, M., Bergeron, P., Dame, K., Hambly, N. C., Rowell, N., and Crawford, C. L. (2019). The age of the Galactic stellar halo from Gaia white dwarfs. MNRAS, 482:965–979.

Kleinman, S. J., Harris, H. C., Eisenstein, D. J., Liebert, J., Nitta, A., Krzesiński, J., Munn, J. A., Dahn, C. C., Hawley, S. L., Pier, J. R., Schmidt, G., Silvestri, N. M., Smith, J. A., Szkody, P., Strauss, M. A., Knapp, G. R., Collinge, M. J., Mukadam, A. S., Koester, D., Uomoto, A., Schlegel, D. J., Anderson, S. F., Brinkmann, J., Lamb, D. Q., Schneider, D. P., and York, D. G. (2004). A Catalog of Spectroscopically Identified White Dwarf Stars in the First Data Release of the Sloan Digital Sky Survey. ApJ, 607(1):426–444.

Kleinman, S. J., Kepler, S. O., Koester, D., Pelisoli, I., Peçanha, V., Nitta, A., Costa, J. E. S., Krzesinski, J., Dufour, P., Lachapelle, F.-R., Bergeron, P., Yip, C.-W., Harris, H. C., Eisenstein, D. J., Althaus, L., and Córsico, A. (2013). SDSS DR7 White Dwarf Catalog. ApJS, 204:5.

Koester, D. (2010). White dwarf spectra and atmosphere models . Mem. Soc. Astron. Italiana, 81:921–931.

Kouwenhoven, M. B. N., Goodwin, S. P., Parker, R. J., Davies, M. B., Malmberg, D., and Kroupa, P. (2010). The formation of very wide binaries during the star cluster dissolution phase. MNRAS, 404:1835–1848.

Lachaume, R., Dominik, C., Lanz, T., and Habing, H. J. (1999). Age determinations of main-sequence stars: combining different methods. A&A, 348:897–909.

Lépine, S. (2005). Nearby Stars from the LSPM-North Proper-Motion Catalog. I. Main-Sequence Dwarfs and Giants within 33 Parsecs of the Sun. AJ, 130:1680–1692.

Li, T., Bedding, T. R., Christensen-Dalsgaard, J., Stello, D., Li, Y., and Keen, M. A. (2020). Asteroseismology of 36 Kepler subgiants - II. Determining ages from detailed modelling. MNRAS, 495(3):3431–3462.

Luo, A. L., Zhao, Y.-H., Zhao, G., Deng, L.-C., Liu, X.-W., Jing, Y.-P., Wang, G., Zhang, H.-T., Shi, J.-R., Cui, X.-Q., Chu, Y.-Q., Li, G.-P., Bai, Z.-R., Wu, Y., Cai, Y., Cao, S.-Y., Cao, Z.-H., Carlin, J. L., Chen, H.-Y., Chen, J.-J., Chen, K.-X., Chen, L., Chen, X.-L., Chen, X.-Y., Chen, Y., Christlieb, N., Chu, J.-R., Cui, C.-Z., Dong, Y.-Q., Du, B., Fan, D.-W., Feng, L., Fu, J.-N., Gao, P., Gong, X.-F., Gu, B.-Z., Guo, Y.-X., Han, Z.-W., He, B.-L., Hou, J.-L., Hou, Y.-H., Hou, W., Hu, H.-Z., Hu, N.-S., Hu, Z.-W., Huo, Z.-Y., Jia, L., Jiang, F.-H., Jiang, X., Jiang, Z.-B., Jin, G., Kong, X., Kong, X., Lei, Y.-J., Li, A.-H., Li, C.-H., Li, G.-W., Li, H.-N., Li, J., Li, Q., Li, S., Li, S.-S., Li, X.-N., Li, Y., Li, Y.-B., Li, Y.-P., Liang, Y., Lin, C.-C., Liu, C., Liu, G.-R., Liu, G.-Q., Liu, Z.-G., Lu, W.-Z., Luo, Y., Mao, Y.-D., Newberg, H., Ni, J.-J., Qi, Z.-X., Qi, Y.-J., Shen, S.-Y., Shi, H.-M., Song, J., Song, Y.-H., Su, D.-Q., Su, H.-J., Tang, Z.-H., Tao, Q.-S., Tian, Y., Wang, D., Wang, D.-Q., Wang, F.-F., Wang, G.-M., Wang, H., Wang, H.-C., Wang, J., Wang, J.-N., Wang, J.-L., Wang, J.-P., Wang, J.-X., Wang, L., Wang, M.-X., Wang, S.-G., Wang, S.-Q., Wang, X., Wang, Y.-N., Wang, Y., Wang, Y.-F., Wang, Y.-F., Wei, P., Wei, M.-Z., Wu, H., Wu, K.-F., Wu, X.-B., Wu, Y.-Z., Xing, X.-Z., Xu, L.-Z., Xu, X.-Q., Xu, Y., Yan, T.-S., Yang, D.-H., Yang, H.-F., Yang, H.-Q., Yang, M., Yao, Z.-Q., Yu, Y., Yuan, H., Yuan, H.-B., Yuan, H.-L., Yuan, W.-M., Zhai, C., Zhang, E.-P., Zhang, H.-W., Zhang, J.-N., Zhang, L.-P., Zhang, W., Zhang, Y., Zhang, Y.-X., Zhang, Z.-C., Zhao, M., Zhou, F., Zhou, X., Zhu, J., Zhu, Y.-T., Zou, S.-C., and Zuo, F. (2015). The first data release (DR1) of the LAMOST regular survey. *Research in Astronomy and Astrophysics*, 15(8):1095.

Michalik, D., Lindegren, L., and Hobbs, D. (2015). The Tycho-Gaia astrometric solution . How to get 2.5 million parallaxes with less than one year of Gaia data. A&A, 574:A115.

Nordström, B., Mayor, M., Andersen, J., Holmberg, J., Pont, F., Jørgensen, B. R., Olsen, E. H., Udry, S., and Mowlavi, N. (2004). The Geneva-Copenhagen survey of the Solar neighbourhood. Ages, metallicities, and kinematic properties of 14 000 F and G dwarfs. A&A, 418:989–1019.

Paxton, B., Bildsten, L., Dotter, A., Herwig, F., Lesaffre, P., and Timmes, F. (2011). Modules for Experiments in Stellar Astrophysics (MESA). ApJS, 192:3.

Paxton, B., Cantiello, M., Arras, P., Bildsten, L., Brown, E. F., Dotter, A., Mankovich, C., Montgomery, M. H., Stello, D., Timmes, F. X., and Townsend,

R. (2013). Modules for Experiments in Stellar Astrophysics (MESA): Planets, Oscillations, Rotation, and Massive Stars. ApJS, 208:4.

Paxton, B., Marchant, P., Schwab, J., Bauer, E. B., Bildsten, L., Cantiello, M., Dessart, L., Farmer, R., Hu, H., Langer, N., Townsend, R. H. D., Townsley, D. M., and Timmes, F. X. (2015). Modules for Experiments in Stellar Astrophysics (MESA): Binaries, Pulsations, and Explosions. ApJS, 220:15.

Ramírez, I., Allende Prieto, C., and Lambert, D. L. (2013). Oxygen Abundances in Nearby FGK Stars and the Galactic Chemical Evolution of the Local Disk and Halo. ApJ, 764(1):78.

Ramírez, I., Allende Prieto, C., Redfield, S., and Lambert, D. L. (2006). Fundamental parameters and abundances of metal-poor stars: the SDSS standard BD +17 4708. A&A, 459(2):613–625.

Ramírez, I., Meléndez, J., Bean, J., Asplund, M., Bedell, M., Monroe, T., Casagrande, L., Schirbel, L., Dreizler, S., Teske, J., Tucci Maia, M., Alves-Brito, A., and Baumann, P. (2014). The Solar Twin Planet Search. I. Fundamental parameters of the stellar sample. A&A, 572:A48.

Renedo, I., Althaus, L. G., Miller Bertolami, M. M., Romero, A. D., Córsico, A. H., Rohrmann, R. D., and García-Berro, E. (2010). New Cooling Sequences for Old White Dwarfs. ApJ, 717:183–195.

Romero, A. D., Campos, F., and Kepler, S. O. (2015). The age-metallicity dependence for white dwarf stars. MNRAS, 450(4):3708–3723.

Silvestri, N. M., Oswalt, T. D., Wood, M. A., Smith, J. A., Reid, I. N., and Sion, E. M. (2001). White Dwarfs in Common Proper Motion Binary Systems: Mass Distribution and Kinematics. AJ, 121:503–516.

Sneden, C. A. (1973). *Carbon and Nitrogen Abundances in Metal-Poor Stars.* PhD thesis, THE UNIVERSITY OF TEXAS AT AUSTIN.

Soubiran, C., Jasniewicz, G., Chemin, L., Zurbach, C., Brouillet, N., Panuzzo, P., Sartoretti, P., Katz, D., Le Campion, J.-F., Marchal, O., Hestroffer, D., Thévenin, F., Crifo, F., Udry, S., Cropper, M., Seabroke, G., Viala, Y., Benson, K., Blomme, R., Jean-Antoine, A., Huckle, H., Smith, M., Baker, S. G., Damerdji, Y., Dolding, C., Frémat, Y., Gosset, E., Guerrier, A., Guy, L. P., Haigron, R., Janßen, K., Plum, G., Fabre, C., Lasne, Y., Pailler, F., Panem, C., Riclet, F., Royer, F., Tauran, G., Zwitter, T., Gueguen, A., and Turon, C. (2018). Gaia Data Release 2. The catalogue of radial velocity standard stars. A&A, 616:A7.

Soubiran, C., Le Campion, J.-F., Brouillet, N., and Chemin, L. (2016). The PASTEL catalogue: 2016 version. A&A, 591:A118.

Stetson, P. B. and Pancino, E. (2008). DAOSPEC: An Automatic Code for Measuring Equivalent Widths in High-Resolution Stellar Spectra. PASP, 120(874):1332.

Vassiliadis, E. and Wood, P. R. (1993). Evolution of Low- and Intermediate-Mass Stars to the End of the Asymptotic Giant Branch with Mass Loss. ApJ, 413:641.

Weidemann, V. (1977). Mass loss towards the white dwarf stage. A&A, 59:411–418.

Weidemann, V. (1993). Integrated Mass Loss on the AGB. In *European Southern Observatory Conference and Workshop Proceedings*, volume 46 of *European Southern Observatory Conference and Workshop Proceedings*, page 55.

Weidemann, V. (2000). Revision of the initial-to-final mass relation. A&A, 363:647–656.

Weiss, A. and Ferguson, J. W. (2009). New asymptotic giant branch models for a range of metallicities. A&A, 508:1343–1358.

Williams, K. A., Bolte, M., and Koester, D. (2009). Probing the Lower Mass Limit for Supernova Progenitors and the High-Mass End of the Initial-Final Mass Relation from White Dwarfs in the Open Cluster M35 (NGC 2168). ApJ, 693:355–369.

Yi, S., Demarque, P., Kim, Y.-C., Lee, Y.-W., Ree, C. H., Lejeune, T., and Barnes, S. (2001). Toward Better Age Estimates for Stellar Populations: The Y^2 Isochrones for Solar Mixture. ApJS, 136:417–437.

Yoo, J., Chanamé, J., and Gould, A. (2004). The End of the MACHO Era: Limits on Halo Dark Matter from Stellar Halo Wide Binaries. ApJ, 601(1):311–318.

Zhao, J. K., Oswalt, T. D., Willson, L. A., Wang, Q., and Zhao, G. (2012). The Initial-Final Mass Relation among White Dwarfs in Wide Binaries. ApJ, 746:144.